

Families of Two-Impulse Optimal Rendezvous Transfers Between Elliptic Orbits

Beom Park* and Kathleen C. Howell[†],
School of Aeronautics and Astronautics, Purdue University, West Lafayette, IN, 47906

Jaewoo Kim[‡] and Jaemyung Ahn[§]
Korea Advanced Institute of Science and Technology, Daejeon, 34141, Republic of Korea

The classical fuel-optimal two-impulse rendezvous problem between Keplerian orbits is revisited from a family-based perspective. Conventional approaches often yield isolated optimal solutions whose mutual relationships remain unclear; yet, when re-parameterized appropriately, seemingly unrelated optima are revealed to be connected members of continuous solution families. To expose this structure, the proposed framework enforces a subset of first-order necessary optimality conditions and traces the resulting one-parameter families via numerical continuation. The families are classified using Hessian-based criteria and Primer Vector Theory, and are projected onto porkchop plots to connect the angular and temporal domains. Representative case studies reveal the emergence, merging, and disappearance of locally optimal branches under variations in orbital geometry, supplying a global map of the solution landscape. This complementary perspective clarifies the robustness of optimal solutions and identifies alternative near-optimal transfers in the vicinity of a nominal trajectory.

I. Introduction

Since the dawn of spaceflight, fuel-optimal trajectories between Keplerian orbits have held both practical and theoretical significance. The most fundamental example is the Hohmann transfer [1], representing the simplest case of a two-impulse maneuver connecting coplanar circular orbits without rendezvous constraints. Any relaxation of these assumptions, whether in orbital geometry, thrust model, or mission constraints, rapidly increases analytical complexity and has motivated decades of research [2–4]. For instance, generalizations may allow for arbitrary eccentricities or inclinations [5]. The number of burns may also vary; bi-elliptic transfers, for example, can outperform the Hohmann transfer when large energy or plane changes are required [6]. Introducing finite-thrust propulsion rather than impulsive burns further expands the feasible design space, significantly complicating the optimization problem [7, 8]. Furthermore, higher-fidelity dynamical models, such as those required for the cislunar environment [9] or bodies with significant

*Apollo 11 Postdoctoral Fellow, park1103@purdue.edu.

[†]Hsu Lo Distinguished Professor, howell@purdue.edu, AIAA Fellow.

[‡]PhD Candidate, Department of Aerospace Engineering, 291 Daehak-ro; jw.kim@kaist.ac.kr. Student Member AIAA (Corresponding Author).

[§]Professor of Aerospace Engineering, 291 Daehak-ro; jaemyung.ahn@kaist.ac.kr. AIAA Associate Fellow.

oblateness [10], often render fuel-optimal strategies derived from two-body assumptions insufficient. Conversely, within linearized dynamical regimes, simplified analytical formulations remain valuable and have fostered numerous framework developments, e.g., [11, 12].

Despite these extensive generalizations of fuel-optimal trajectory design, the current analysis returns to one of the most fundamental yet still incompletely understood scenarios: the Two-Impulse fuel-Optimal rendezvous Transfers (TIOTs) between general elliptic, Keplerian orbits. The importance of this configuration cannot be overstated; it represents the simplest mission architecture, characterized by short transfer times and analytical tractability, while still exhibiting rich and nontrivial optimal structures. As noted by Saloglu et al. [13] and Saloglu and Taheri [14], TIOTs form the building blocks of more complex multiple-impulse solutions. Similarly, low-thrust transfers may also be continued from these simple impulsive-burn optimal trajectories [15]. Therefore, understanding their organization, bifurcations, and global behaviors remains essential for extending insights to broader mission scenarios.

The following example illustrates that TIOTs, although locally optimal and widely separated in the conventional time-domain representation, may share a common geometric origin. Consider a sample transfer scenario between two elliptic orbits centered around Earth (Table 1). Figure 1(a) displays the total cost of two impulsive burns (J)* over departure time (T) and flight time (t); four local optimal solutions (colored markers) appear widely separated in the time domain. However, when re-parameterized by the angular positions along each orbit (Fig. 1(c)), these solutions cluster tightly, revealing that they belong to a continuous family sharing similar transfer geometries (Fig. 1(b)). This observation, that seemingly isolated optima are in fact connected members of a broader family, motivates the present framework.†

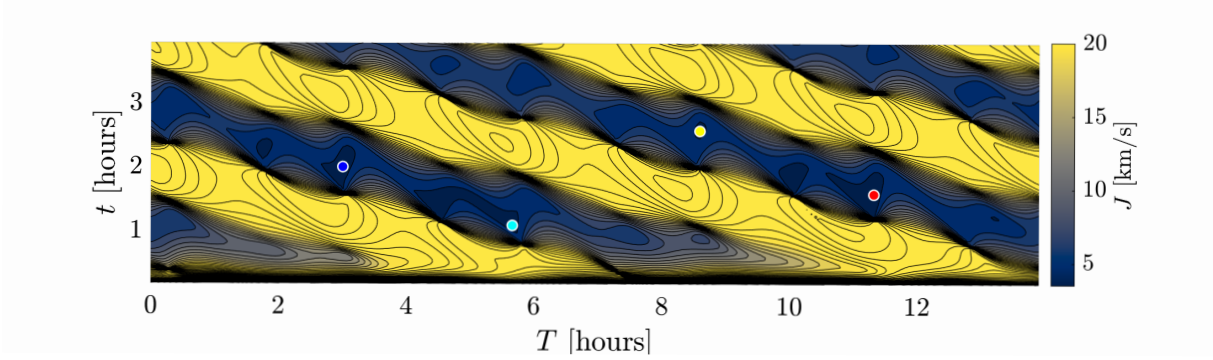
Table 1 Orbital elements defining the baseline transfer case between two Keplerian orbits in an Earth-centered inertial frame (notation is formally defined in Section II)

Orbit	a [km]	e [-]	i [deg]	Ω [deg]	ω [deg]	M^0 [deg]
Orbit 1 (Departure)	10000	0.1	0°	0°	0°	0°
Orbit 2 (Arrival)	8000	0.1	30°	45°	45°	0°

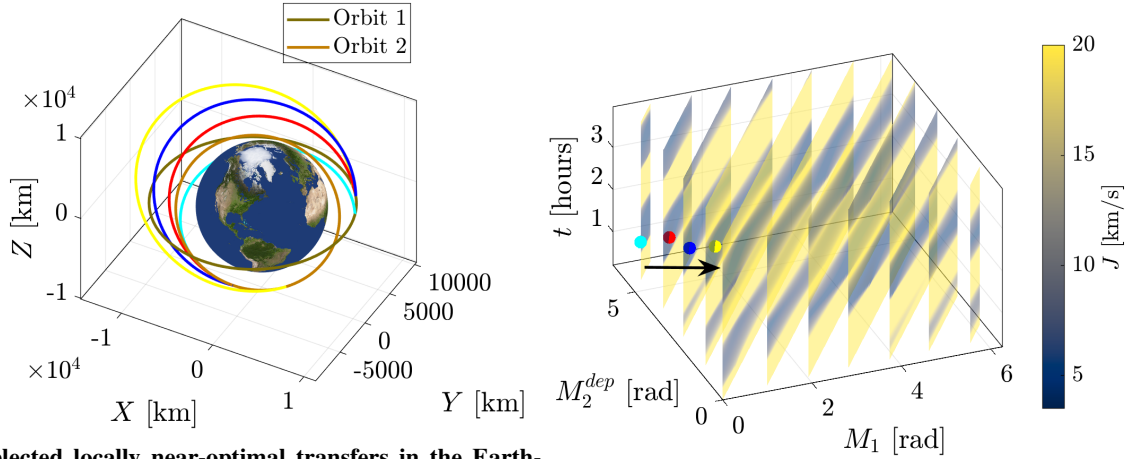
Motivated by this observation, the current study develops a framework that systematically identifies and traces such families of TIOTs between general elliptic orbits. By enforcing a subset of first-order necessary optimality conditions, the methodology reduces the three-dimensional search space to a one-parameter continuation problem, connecting isolated local minima into continuous solution curves. The resulting families reveal the global organization of optimal transfers, including the coalescence, emergence, and disappearance of distinct branches as orbital geometry varies, and

*All Lambert arcs in this example are zero-revolution with transfer angle exceeding 180° (long-way); these parameters are formally defined in Section II.

†The quasi-periodic recurrence of favorable transfer geometries is well established in planetary mission design (e.g., Earth–Mars synodic windows) and has long informed heuristic search strategies for TIOTs in long-horizon planning contexts, e.g., Bang and Ahn [16]; however, a systematic global characterization of the underlying solution structure has remained largely absent.



(a) Cost landscape over departure epoch and flight time (markers indicate locally near-optimal transfers).



(b) Selected locally near-optimal transfers in the Earth-centered inertial frame (all trajectories are prograde, i.e., $i < 90^\circ$).

(c) Cost landscape re-parameterized by departure and arrival mean anomalies (M_1, M_2^{dep}) and flight time.

Fig. 1 Cost landscape and selected transfer geometries for the baseline transfer scenario (Table 1).

supply a natural basis for assessing solution robustness. By projecting these families onto the temporal domain, the framework further connects to conventional porkchop-plot analyses, bridging geometric insight with epoch-specific mission planning.

The remainder of this paper is organized as follows. Section II introduces the preliminaries, including the Lambert problem formulation and a summary of existing TIOT strategies. Sections III–V present the proposed methodology: Section III defines *families* of TIOTs and formalizes the relationships among family members under a generalized notion of optimality; Section IV defines two optimality domains (angular and temporal), characterizes their asymptotic behavior, and establishes the correspondence between the two formulations; and Section V describes the numerical procedure used to identify and analyze TIOT families. Section VI applies the framework to multiple departure–arrival orbit pairs to illustrate its use and to extract case-based insights. Finally, Section VII concludes the paper.

II. Background

This section provides the background for the present study. The Lambert problem, a key building block for TIOT solutions, is first introduced along with the nomenclature and conventions used throughout. Three established classes of TIOT strategies are then reviewed: (1) geometry-based analysis, (2) numerical optimization, and (3) Primer Vector Theory (PVT).

A. Problem Formulation

The TIOT problem between two elliptic orbits is introduced. The fixed orbital elements of the departure and arrival ellipses are denoted as,

$$\boldsymbol{\alpha}_j = [a_j, e_j, i_j, \Omega_j, \omega_j]^\top, \quad \text{for } j = 1, 2, \quad (1)$$

where the symbols a, e, i, Ω, ω represent the classical orbital elements, i.e., semi-major axis, eccentricity, inclination, right ascension of the ascending node, and the argument of periapsis, respectively, defined within an arbitrary inertial frame. While the formulation extends to any central body, the current investigation primarily focuses on Earth-centered scenarios. Subscripts 1, 2 correspond to the departure and arrival, respectively. The sixth element specifies the location of the spacecraft along the orbit. Mean anomalies are mainly adopted in the current work, i.e.,

$$M_1 = n_1 T + M_1^0, \quad (2)$$

$$M_2^{dep} = n_2 T + M_2^0, \quad (3)$$

$$M_2 = n_2(T + t) + M_2^0, \quad (4)$$

where n_i is the mean motion supplied from a_i , T is time measured from an arbitrary reference time, and M_i^0 is the mean anomaly at the arbitrary reference time. The two-impulsive burn rendezvous transfer leads to one transfer conic; denote the transfer time (time-of-flight) as t . Note that M_2^{dep}, M_2 refer to mean anomalies upon the departure time (T) and arrival time ($T + t$), respectively. Thus, the transfer arc links the position vectors along the departure and arrival ellipses at,

$$\mathbf{r}_1 = \mathbf{r}_1(T) = \mathbf{r}_1(T; \boldsymbol{\alpha}_1, M_1^0), \quad (5)$$

$$\mathbf{r}_2 = \mathbf{r}_2(T + t) = \mathbf{r}_2(T + t; \boldsymbol{\alpha}_2, M_2^0), \quad (6)$$

defined in an inertial frame. Finding a transfer arc satisfying the boundary constraints (Eqs. (5)-(6)) under Keplerian dynamics with a specified time-of-flight t constitutes the Lambert problem [17]. It solves for a transfer conic Γ defined

as,

$$\Gamma = \Gamma(\mathbf{r}_1, \mathbf{r}_2, t; \mu, N, d_1, d_2). \quad (7)$$

The gravitational parameter of the central celestial body is denoted as μ . The number of revolutions is N , defined as $N = \lfloor \theta / (2\pi) \rfloor$ with θ denoting the change in true anomaly along the Lambert arc Γ . The switch d_1 resolves the ambiguity in θ and $2\pi - \theta$ for a given set of \mathbf{r}_1 and \mathbf{r}_2 ; $d_1 \in \{s, l\}$ denotes short and long transfers with $0 < \theta - 2N\pi < \pi$ and $\pi < \theta - 2N\pi < 2\pi$, respectively. The last parameter $d_2 \in \{0, 1\}$ resolves the additional geometrical ambiguity that arises in transfers with $N \geq 1$; for a given N , two distinct transfer ellipses connect the same boundary positions in the same flight time, differing in their semi-major axes. Following Russell [18], d_2 distinguishes these two solutions by the location of the second focus of the transfer ellipse relative to the chord line. Then, the cost of the two-impulsive burn rendezvous trajectories renders,

$$J := |\Delta \mathbf{v}_1| + |\Delta \mathbf{v}_2|, \quad (8)$$

where 1, 2 are subscripts for the burns at the departure and final orbits. The difference in the velocity vector constitutes the impulsive burns as,

$$\Delta \mathbf{v}_1 = \mathbf{v}_1^\Gamma - \mathbf{v}_1, \quad \Delta \mathbf{v}_2 = \mathbf{v}_2 - \mathbf{v}_2^\Gamma, \quad (9)$$

where \mathbf{v}_1 and \mathbf{v}_2 are velocity vectors along the departure and arrival orbits and \mathbf{v}_1^Γ and \mathbf{v}_2^Γ are velocity vectors along the Lambert arc Γ at the initial and final times, i.e., T and $T + t$, respectively. For a fixed set of departure and arrival orbital elements, the cost function consists of the following independent variables and parameters,

$$J = J(T, t; \mathbf{a}_1, M_1^0, \mathbf{a}_2, M_2^0, \mu, N, d_1, d_2). \quad (10)$$

It is typical to analyze different combinations for N, d_1, d_2 as they constitute discrete parameters. In the current analysis, $N = 0$ is analyzed, establishing the simplest case. For brevity, the parameters $(\mathbf{a}_1, M_1^0, \mathbf{a}_2, M_2^0, \mu, N, d_2)$ are omitted in the expressions in the rest of the document as they are fixed values in the current analysis, leaving dependency only on $d_1 \in \{s, l\}$. Utilizing the relationship between the time and angles from Eqs. (2)-(4), the cost is alternatively represented as,

$$J = J(T, t; d_1) = J(M_1, M_2, t; d_1) = J(M_1, M_2^{dep}, t; d_1). \quad (11)$$

The alternative domains with angles aid the extraction of patterns, as demonstrated later. Consequently, the problem of locating TIOTs is defined as finding the set of independent variables that (locally) minimizes the cost function J .

Lambert solvers serve as the foundation for any two-impulse rendezvous problem, since Eq. (8) requires solving Eq. (7). Although a general closed-form solution does not exist, Keplerian dynamics allows for geometric and semi-analytical exploration. While a comprehensive review lies beyond the scope of this work, notable contributions warrant acknowledgment. Research in this domain generally centers on two aspects: (1) computational efficiency and (2) algorithmic robustness. Singularities within the Lambert problem often impede the successful construction of the solution, motivating continuous improvements toward faster and more robust formulations. Following Lambert’s initial formulation and Lagrange’s derivation of the time-of-flight equations, modern contributions emerge from Lancaster and Blanchard [19]. Battin [17] emphasizes iterative techniques with improved convergence properties. Gooding [20] develops a fast, robust method with guaranteed convergence using a universal variable approach, while Izzo [21] proposes an efficient algorithm utilizing variable transformation and root-finding on a bounded domain. This study adopts Izzo’s [21] formulation for the internal Lambert arc routine.

B. Locating TIOTs: Existing Strategies

Existing literature on TIOTs can be broadly categorized into three approaches: (1) geometry-based analysis, (2) numerical optimization, and (3) Primer Vector Theory (PVT). This section reviews each in turn, highlighting their respective contributions and limitations.

1. Geometry-Based Analysis

By harnessing the geometric properties of the departure, arrival, and transfer orbits, this approach aims for a (semi-)analytical characterization of TIOTs. A divide-and-conquer strategy is typically adopted, starting with simplifying assumptions that are gradually lifted in subsequent research. For example, the Hohmann transfer [1] constitutes the simplest scenario with two coplanar, circular orbits, admitting a proven globally optimal solution [22–24]. Transfers involving inclined circular orbits are discussed in Baker [25], while optimal transfers between coplanar ellipses are detailed in Pontani [26] and Zaborsky [27]. In these analyses, bi-elliptic transfers serve as a competing option, augmenting the optimality landscape. However, to the authors’ best knowledge, analytical criteria for locating optimal transfers within the most general formulation, involving non-coplanar, non-coaxial ellipses, remain elusive. In such complex configurations, geometric heuristics are often examined as proxies for true optimal solutions. For example, Vinh et al. [5] investigate the optimal “nodal” transfer, where two impulsive burns are placed on the common line of nodes; such a configuration is also analyzed in Baker [25] and denoted as “modified Hohmann transfer.” Likewise, Lacruz and Ángeles [28] examine transfer geometries with certain properties, e.g., coaxial with the departure or arrival orbits.

2. Numerical Methods: Grid Search and Optimization

Advances in Lambert solvers [18, 21, 29, 30] enable large-scale parametric searches and visualizations such as porkchop plots. The porkchop plot serves as the de facto graphical strategy for surveying the solution space. The grid typically spans the (T, t) domain, or equivalently, the $(T, T + t)$ domain, where the Lambert arcs and resulting costs J are evaluated iteratively. For example, recall the baseline transfer scenario (Table 1)[‡]. The synodic period of the two orbits is approximately $P_{syn} = 2\pi/(n_2 - n_1) \approx 7$ hours. The porkchop plot in Fig. 1(a) is generated for $N = 0$ and $d_1 = 1$ (long transfer, $\pi < \theta < 2\pi$), with $0 \leq T \leq 2P_{syn}$ and $0.2 \leq t \leq 4$ hours over a 200×100 grid. The colormap represents the cost J defined in Eq. (8), where darker blue regions correspond to locally optimal Lambert arcs connecting the two orbits. Although grid search provides a global view of the cost landscape, its limited sampling resolution may not capture all locally optimal solutions, and the resulting patterns offer limited insight into the connectivity and continuity of optimal configurations.

Various optimization approaches supply another numerical route for locating TIOTs. In early works, McCue [31] and Lee [32] partially enforce necessary optimality conditions to generate contours and analytical insights, while McCue [33] applies a gradient descent algorithm to locate locally optimal solutions. These optimization efforts are closely tied to geometry-based analysis, as the necessary optimality conditions yield polynomial expressions derived from orbital geometry [32, 34]. More recently, Bang and Ahn [16] employ a gradient-based search initialized from grid samples, and meta-heuristic optimization schemes [35, 36] reduce reliance on the initial grid. Gradient-based methods [33, 37] typically offer faster convergence but risk entrapment in local minima, whereas meta-heuristic approaches increase the likelihood of identifying globally optimal solutions at a higher computational cost. However, despite their flexibility, these numerical approaches often provide isolated “point” solutions, leaving the physical origins of recurring patterns in the cost landscape opaque.

3. Primer Vector Theory (PVT)

Lawden’s PVT [7] supplies an analytical framework for verifying the optimality of impulsive trajectories, complementary to the geometry-based and numerical approaches above. Under the impulsive thrust assumption, the costate vector $[\lambda_r^\top, \lambda_v^\top]^\top$ is augmented to the state vector, i.e., $[r^\top, v^\top]^\top$. Then, the “primer vector” is defined as $\mathbf{p} = -\lambda_v$. According to Lawden’s theory [7], an optimal impulsive trajectory must satisfy four necessary conditions regarding \mathbf{p} and its time derivative $d\mathbf{p}/d\tau$ [§]: (1) \mathbf{p} and $d\mathbf{p}/d\tau$ must be continuous throughout the transfer, (2) the magnitude of the primer vector must not exceed unity ($|\mathbf{p}| \leq 1$) at any point along the trajectory, (3) at the instants of impulsive burns, the primer vector must be a unit vector aligned with the thrust direction (i.e., $\mathbf{p} = \Delta\mathbf{v}/|\Delta\mathbf{v}|$ and $|\mathbf{p}| = 1$), and (4) if an intermediate coast arc exists between impulses, the derivative of the primer vector magnitude must vanish

[‡]Unless otherwise stated, all numerical examples and family analyses in this study are referenced to the baseline transfer case defined in Table 1.

[§]The generic independent variable for time is τ , differentiated from the transfer parameters T, t .

($d|\mathbf{p}|/d\tau = 0$) at any interior point where $|\mathbf{p}| = 1$. While applicable to general dynamical regimes, the specific equations of motion for Keplerian dynamics are briefly recalled as,

$$\frac{d\mathbf{r}}{d\tau} = \mathbf{v}, \quad (12)$$

$$\frac{d\mathbf{v}}{d\tau} = \mathbf{g}(\mathbf{r}) = -\frac{\mu}{r^3}\mathbf{r}. \quad (13)$$

From optimal control theory [8], the costates evolve according to

$$\frac{d\lambda_r}{d\tau} = -\mathbf{G}\lambda_v, \quad (14)$$

$$\frac{d\lambda_v}{d\tau} = -\lambda_r, \quad (15)$$

where $\mathbf{G} = \frac{\partial \mathbf{g}}{\partial \mathbf{r}} = \frac{\mu}{r^5}(3\mathbf{r}\mathbf{r}^\top - r^2\mathbf{I})$ and \mathbf{I} is a three-by-three identity matrix. The distinct advantage of PVT over parametric optimization lies in determining the optimal number of impulses. While the parametric framework typically assumes a fixed number of burns, PVT provides analytical criteria indicating whether intermediate burns would further reduce fuel costs. Building on Lawden's foundation, the literature extends PVT to multiple-impulse transfers [38], multi-revolution cases [39], and the convergence of finite-thrust trajectories toward impulsive solutions; Taheri and Junkins [40] demonstrate that finite-thrust solutions converge to these impulsive limits, confirming the physical significance of the necessary conditions. Consequently, this analysis leverages PVT as a complementary tool to post-assess the optimality of converged solutions from parametric optimization. However, PVT remains inherently local; it verifies the optimality of individual trajectories but does not directly reveal the global topology or connectivity of solution families.

III. Optimization Formulation and Solution Dimensionality

This section formulates the optimization problem for two-impulse transfers and introduces a continuation framework for tracing one-dimensional families of TIOTs. Section III.A motivates the adoption of angular variables over the conventional time domain, Section III.B defines the continuation scheme based on partial optimality conditions, and Section III.C details the required gradient information and the Hessian-based classification of stationary solutions.

A. Motivation and Dimensionality

The optimization of two-impulse transfers between elliptic orbits is inherently governed by three design variables [31]. This three-dimensional domain consists of the (1) departure and (2) arrival locations along the respective orbits and the (3) geometry of the transfer arc, often parameterized by the semi-latus rectum or, equivalently, the time-of-flight. In the present formulation, this three-dimensional domain is represented by the state vector $\mathbf{X} = [M_1, M_2, t]^\top$. Consequently,

the cost J constitutes a scalar field over this three-dimensional space.

As discussed in Section II, directly solving the full optimization problem (i.e., enforcing $\nabla J = \mathbf{0}$) yields isolated point solutions, offering limited insight into the global solution structure. Beyond this limitation, the choice of independent variables fundamentally dictates the representation of these optimal structures. While the two angles M_1 and M_2 (or, M_2^{dep}) are bounded between $[0, 2\pi)$, such angles unravel as a function of T , recalling the alternative representations of J from Eq. (11). Consequently, the typical time domain, (T, t) , is often inadequate for revealing the underlying connectivity of solution families. The unraveling of the periodic angular domain into an infinite time axis effectively fragments continuous structures into isolated points, obscuring their relationships. In the time domain, the locally optimal solutions satisfy the first-order necessary conditions,

$$\frac{\partial J}{\partial T} = \frac{\partial J}{\partial t} = 0. \quad (16)$$

As previewed in Fig. 1, four such solutions appear widely separated in the (T, t) space yet collapse into a compact neighborhood when re-parameterized by mean anomalies (M_1, M_2^{dep}, t) , confirming that they belong to a continuous family with shared transfer geometries. This observation motivates the present framework to navigate the solution space directly within the $M_1 - M_2 - t$ domain.

B. Families of TIOTs

Building on the motivation from Section III.A, a numerical continuation scheme is devised to trace one-dimensional families of TIOTs within the three-dimensional space. This process leverages a system of nonlinear equations defined over the state vector, $\mathbf{X} = [M_1, M_2, t]^\top$. To generate a continuous family, strictly two optimality conditions are enforced, leaving one degree of freedom unconstrained. With $x_1 = x_1(\mathbf{X})$ and $x_2 = x_2(\mathbf{X})$ denoting two linearly independent variables[¶], the constraint vector is defined as,

$$\mathbf{F}(\mathbf{X}) = \left[\frac{\partial J}{\partial x_1}, \frac{\partial J}{\partial x_2} \right]^\top = \mathbf{0}, \quad (17)$$

enforcing the necessary stationary conditions. Then, \mathbf{X}, \mathbf{F} represent an underdetermined system with 2 equations and 3 unknowns. By relaxing one of the three optimality conditions, the solution expands from an isolated point to a one-dimensional family parameterized by the remaining variable[‡]. Given a solution \mathbf{X}^* that satisfies $\mathbf{F}(\mathbf{X}^*) = \mathbf{0}$, the

[¶]The variables x_1 and x_2 are intentionally left generic here; their concrete assignments (e.g., $x_1 = M_1, x_2 = M_2$ or $x_1 = T, x_2 = t$) are specified in Section IV.

[‡]This approach is inspired by McCarthy et al. [41] and also leveraged in Gul et al. [42]; these prior investigations focus on transfers within non-Keplerian dynamics.

Jacobian of the constraints with respect to the state vector renders,

$$\left. \frac{\partial \mathbf{F}}{\partial \mathbf{X}} \right|_{\mathbf{X}^*}. \quad (18)$$

Being a matrix of size 2×3 , the Jacobian generally allows a one-dimensional null space. This null vector ($\mathcal{N}(\mathbf{X}^*)$) informs the linear prediction for the nearby solution along the family as,

$$\mathbf{X}^p = \mathbf{X}^* + ds \cdot \mathcal{N}(\mathbf{X}^*), \quad (19)$$

where the superscript p stands for the ‘‘predicted’’ state and ds is a scalar step size along the null space direction. To resolve this prediction into a valid solution, the constraints in Equation (17) are enforced again via a differential corrections process (e.g., Newton-Raphson method). To render a square system, an ‘‘arclength’’ constraint may be enforced as well,

$$F^A = (\mathbf{X} - \mathbf{X}^*) \cdot \mathcal{N}(\mathbf{X}^*) - ds = 0, \quad (20)$$

explicitly controlling the step size along the null space direction. For more information regarding this ‘‘pseudo-arclength’’ continuation, refer to Seydel [43].

C. Gradient Information

The continuation scheme (Eqs. (19)–(18)) requires derivatives of the cost function J with respect to the state vector \mathbf{X} . The first-order derivatives,

$$\nabla J = \frac{\partial J}{\partial \mathbf{X}} = \left[\frac{\partial J}{\partial M_1}, \frac{\partial J}{\partial M_2}, \frac{\partial J}{\partial t} \right]^T, \quad (21)$$

are evaluated via the State Transition Matrix (STM) along the Lambert arc, following the approach of Schumacher Jr et al. [44] and Arora et al. [45]. Second-order derivatives of J are also required for two purposes: (1) constructing the Jacobian $\partial \mathbf{F} / \partial \mathbf{X}$ in Eq. (18), and (2) classifying stationary solutions. Derivations for both the first- and second-order derivatives are supplied in Appendix A. Regarding the second-order classification, stationary solutions satisfying Eq. (17) may correspond to a minimum, maximum, or saddle of J , as determined by the eigenvalues λ_A and λ_B of the Hessian matrix,

$$\mathbf{H} = \begin{bmatrix} \frac{\partial^2 J}{\partial x_1^2} & \frac{\partial^2 J}{\partial x_1 \partial x_2} \\ \frac{\partial^2 J}{\partial x_1 \partial x_2} & \frac{\partial^2 J}{\partial x_2^2} \end{bmatrix}. \quad (22)$$

Specifically, the arc is classified as minimum ($\lambda_A, \lambda_B > 0$), maximum ($\lambda_A, \lambda_B < 0$), or saddle ($\lambda_A \lambda_B < 0$). Throughout this analysis, different colors denote the Hessian classification as in Table 2. The term TIOT is utilized to collectively denote all stationary solutions satisfying the first-order optimality conditions, regardless of their second-order classification.

Table 2 Classification of stationary solutions based on Hessian information

Optimality	Color
Minimum	●
Maximum	●
Saddle	●

IV. Optimality Domains and Asymptotic Behaviors

Since the relaxed-constraint formulation admits two independent variables x_1 and x_2 (Eq. (17)), the optimization problem admits multiple domain representations. This section investigates two such selections: the “angular domain” ($x_1 = M_1, x_2 = M_2$), offering analytical insights into the global topology and asymptotic behavior of optimal families, and the “temporal domain” ($x_1 = T, x_2 = t$), directly applicable to mission design and porkchop-plot analysis. The two domains are presented sequentially, followed by a discussion of their asymptotic equivalence.

A. Angular Domain ($M_1 - M_2$)

Physically, optimization over the angular domain assumes that any geometric configuration of M_1 and M_2 is accessible given a sufficient time horizon. This formulation effectively decouples the geometric optimization from the specific epoch or waiting time (T). Consequently, the optimality constraints result in,

$$\left[\frac{\partial J}{\partial M_1}, \frac{\partial J}{\partial M_2} \right]^T = \mathbf{0}. \quad (23)$$

While this formulation renders the angular domain somewhat abstract from immediate mission timelines, it offers profound insights into the asymptotic behaviors of optimal families at the limits $t \rightarrow 0, \infty$. The main text focuses on the $t \rightarrow \infty$ case; for details regarding $t \rightarrow 0$, refer to Appendix B.

As the number of revolutions for the Lambert arc is fixed ($N = 0$ in the current work), the limit $t \rightarrow \infty$ implies that the transfer arc asymptotically approaches a parabolic trajectory with respect to the central celestial body, i.e.,

$$\Gamma \rightarrow \Gamma_{\text{para}}(M_1, M_2; d_1) \quad (24)$$

Compared to Eq. (7), the dependency on t is omitted as $t \rightarrow \infty$. Thus, optimal families initiate (or terminate) at

pairs of M_1, M_2 where the cost J constructed with parabolic arcs, is locally stationary; the velocities \mathbf{v}_1^Γ and \mathbf{v}_2^Γ may be constructed semi-analytically following the process detailed in Appendix C. Note that while the time-dependence is removed, the parabolic Lambert arcs retain dependencies on the geometric parameter, d_1 . Figures 2 and 3 present numerical experiments for short and long transfers, respectively, using the baseline scenario from Table 1. In Figs. 2(a) and 3(a), contour plots are generated with a representatively large time-of-flight value of $t = 25 \cdot 10^3$ seconds** to approximate the behavior of $t \rightarrow \infty$. For comparison, Figs. 2(b) and 3(b) display the contours derived analytically using parabolic Lambert arcs via the process in Appendix C. The identified extremals are summarized in Table 3. In denoting each asymptotic case of the optimal Lambert families, the following notation is introduced,

$$\infty_{b,c}^a, \quad (25)$$

where $a \in \{s, l\}$ denotes the short and long transfer scenarios. The optimality is classified in b with m, M, σ signifying the local minimum, maximum, and saddle, respectively. Finally, $c \geq 1$ is the index to enumerate multiple cases under the same category. Two sample Lambert arcs are illustrated in Fig. 4. Crucially, although a finite t is selected for the numerical plots, the topological structures persist as they asymptotically approach the parabolic limit. Consequently, the extrema identified in this parabolic limit (Table 3) are not merely theoretical curiosities; they serve as robust initial seeds for the continuation process described in Section III.B. By initializing at these asymptotic solutions, the optimal families can be systematically traced from the $t \rightarrow \infty$ regime back into the finite time-of-flight domain.

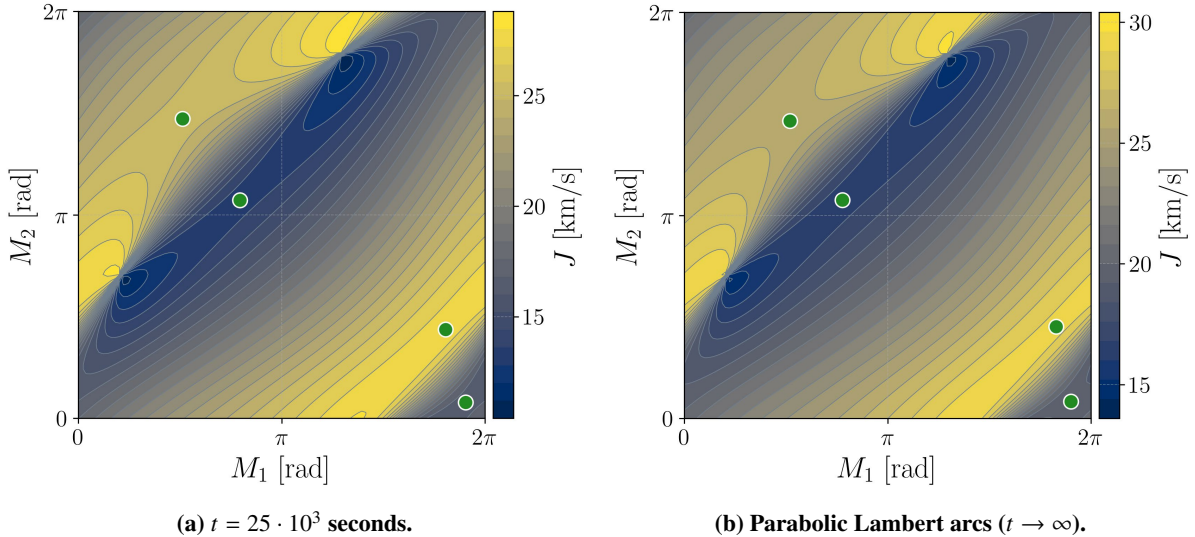


Fig. 2 Comparison of cost landscapes in the angular domain ($d_1 = s$) as $t \rightarrow \infty$. Markers indicate stationary points classified by Hessian information (Table 2).

**For the baseline scenario, this value corresponds to approximately $2.5 P_1$ (or $3.5 P_2$), where P_1 and P_2 denote the orbital periods of the departure and arrival orbits. The specific choice is empirical; any comparably large value yields qualitatively identical contour structures, consistent with the asymptotic convergence toward the parabolic limit.

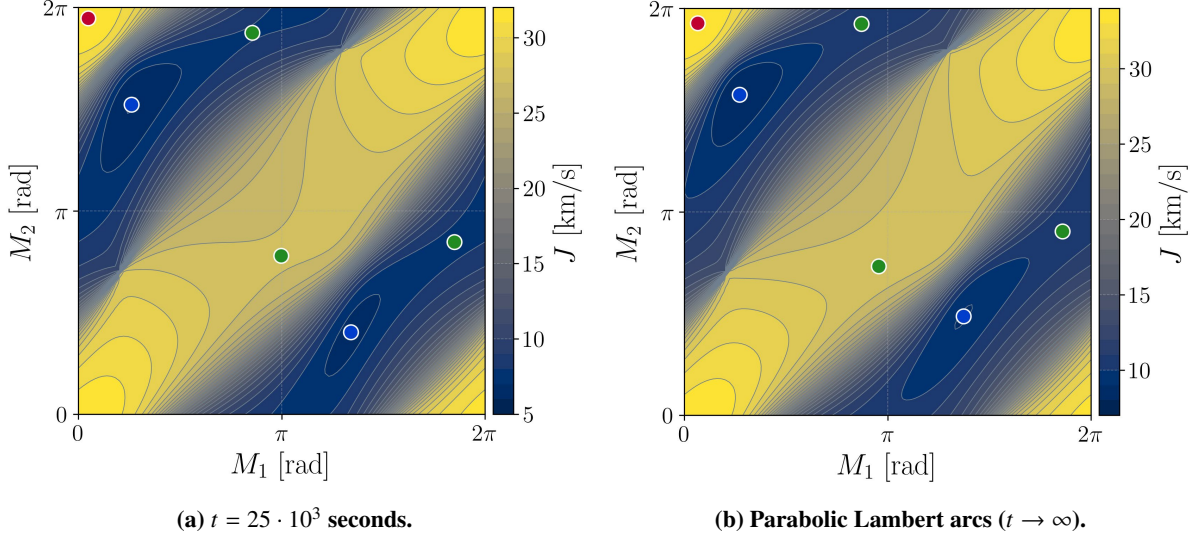


Fig. 3 Comparison of cost landscapes in the angular domain ($d_1 = 1$) as $t \rightarrow \infty$. Markers indicate stationary points classified by Hessian information (Table 2).

Table 3 Asymptotic stationary points ($t \rightarrow \infty$) in the angular domain for the baseline scenario (Table 1)

Label	M_1 [rad]	M_2 [rad]
$\infty_{\sigma,1}^s$	1.63	4.60
$\infty_{\sigma,2}^s$	5.74	1.42
$\infty_{\sigma,3}^s$	2.44	3.38
$\infty_{\sigma,4}^s$	5.98	0.26
$\infty_{M,1}^l$	0.21	6.05
$\infty_{\sigma,1}^l$	3.00	2.30
$\infty_{\sigma,2}^l$	2.73	6.05
$\infty_{\sigma,3}^l$	5.84	2.84
$\infty_{m,1}^l$	0.85	4.95
$\infty_{m,2}^l$	4.31	1.53

B. Temporal domain ($T - t$)

The temporal domain formulation serves as the practical counterpart to the angular domain, directly mapping to the coordinates for standard porkchop plots and mission design. Selecting $x_1 = T$, $x_2 = t$ for Eq. (17) results in the optimality constraint as,

$$\left[\frac{\partial J}{\partial x_1}, \frac{\partial J}{\partial x_2} \right] = \left[\frac{\partial J}{\partial T}, \frac{\partial J}{\partial t} \right] = \mathbf{0}, \quad (26)$$

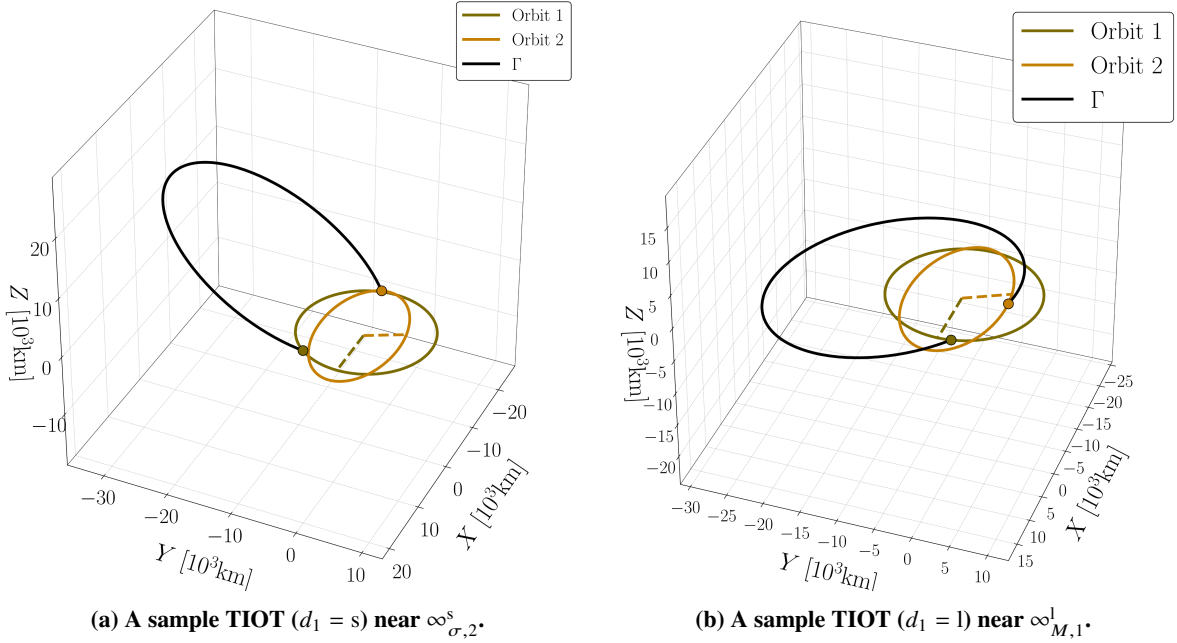


Fig. 4 Representative TIOT geometries in the near-asymptotic regime ($t = 25 \cdot 10^3$ seconds).

with each element derived via the chain rule as,

$$\frac{\partial J}{\partial T} = \frac{\partial J}{\partial M_1} n_1 + \frac{\partial J}{\partial M_2} n_2, \quad (27)$$

$$\frac{\partial J}{\partial t} = \frac{\partial J}{\partial M_2} n_2 + \frac{\delta J}{\delta t}, \quad (28)$$

with the relevant sensitivities supplied in Appendix A. Then, the null space of the Jacobian in Eq. (18) points towards the direction that is perpendicular to the planes in Fig. 1(c). Following this direction enables the exploration of optimal families by effectively decoupling the search from specific epoch constraints, thereby navigating the underlying angular space of M_1 and M_2 . Similar to the angular domain, investigating the asymptotic behavior at $T \rightarrow \infty$ provides critical insights for family initiation. A fundamental question arises: do the analytical structures identified in the angular domain (i.e., parabolic limits) persist in the temporal domain? The following proposition establishes their equivalence,

Proposition 1. *At an asymptotic case $t \rightarrow \infty$, the optimality constraints in the $T - t$ domain (Eqs. (27)-(28)) approach the optimality constraints in the $M_1 - M_2$ domain (Eq. (23)).*

Proof. Refer to Appendix D. □

Consequently, the optimal parabolic transfers identified in the angular domain serve as robust analytical seeds for the temporal domain as well, allowing for the systematic initiation of optimal families from the asymptotic regime.

V. Framework for Families of TIOTs

This section formalizes a computational framework for locating families of TIOTs, building directly on the analytical developments introduced in the preceding sections. The framework consists of three main components: (1) seed initialization, (2) family continuation, and (3) solution analysis. The adoption of this framework enables a systematic exploration of multiple branches of locally optimal transfer solutions between arbitrary departure and arrival orbits. An example transfer scenario, summarized in Table 1, is used throughout this section to illustrate the proposed framework for a representative general rendezvous problem. Among the two optimality domains introduced in Section IV, the temporal domain is the primary focus of the remainder of this work. The framework remains fully applicable to the angular domain; corresponding results are provided in Appendix E.

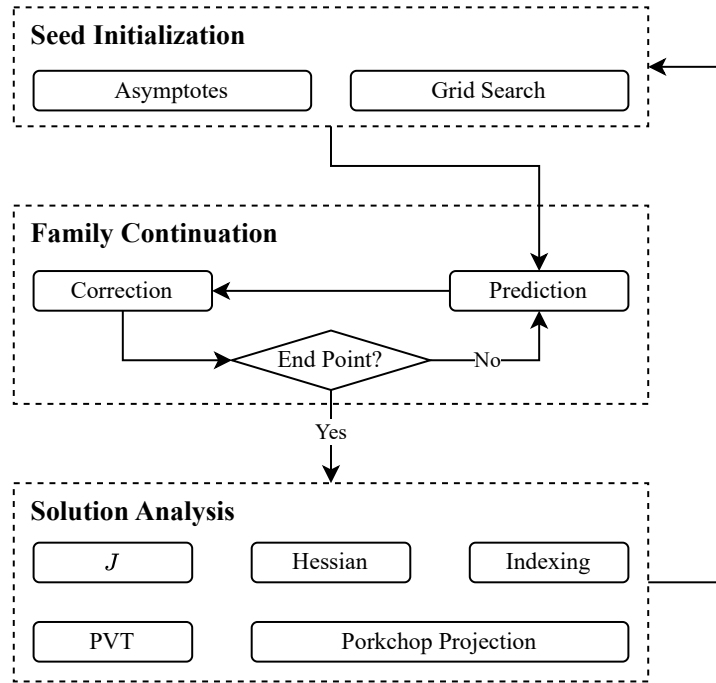


Fig. 5 Conceptual framework for constructing TIOT families.

A. Seed Initialization

To initiate the continuation process described in Section III.B, a set of starting seeds is required. Two complementary approaches are adopted in the present framework: (1) semi-analytic seeds derived from the asymptotic behavior as the time-of-flight approaches infinity, and (2) numerical seeds obtained via grid search. Both strategies are examined concurrently in this investigation. Unlike many previous studies that focus exclusively on minimum-fuel solutions, the present analysis considers all stationary transfers, regardless of their Hessian classification (Section VII.B). This choice is deliberate: along a given family, second-order optimality properties may change, and limiting attention to minima alone may obscure global connectivity between solution branches. By tracking all stationary points and their evolving

families, the framework enables a more complete characterization of the global structure of TIOTs.

1. Seeds from $t \rightarrow \infty$ Asymptotes

The asymptotic behaviors discussed in the preceding section provide a natural source of initial seeds. This approach is semi-analytic, computationally inexpensive, and can be applied without prior knowledge of the detailed structure of a given family. Its applicability, however, is limited to families that originate from or terminate at the asymptotic limit $t \rightarrow \infty$. Families that exhibit closed-loop behavior or remain entirely within finite time-of-flight ranges are not captured by this method.

The asymptotes summarized in Table 3 correspond to parabolic Lambert limits. To generate seeds suitable for continuation at finite time-of-flight, the asymptotic angular configurations are re-converged in the selected optimality domain utilizing a large but finite transfer time. The resulting solutions serve as initial seeds for family continuation in the finite-time regime. For the baseline transfer scenario considered in this study, these seeds are located near $t = 25 \cdot 10^3$ seconds and are listed in Table 4, with labels consistent with their corresponding asymptotic classifications.

Table 4 Re-converged numerical seeds derived from asymptotic stationary points ($t \rightarrow \infty$, Table 3) for family continuation. The seeds are obtained at a representative large time-of-flight ($t \approx 25 \cdot 10^3$ seconds) within the temporal domain.

Root asymptote	M_1 [rad]	M_2 [rad]	t [10^3 sec]
$\infty_{\sigma,1}^s$	1.61	4.64	25.0
$\infty_{\sigma,2}^s$	5.69	1.39	25.1
$\infty_{\sigma,3}^s$	2.46	3.32	25.1
$\infty_{\sigma,4}^s$	5.98	0.24	25.0
$\infty_{M,1}^l$	0.13	6.12	25.2
$\infty_{\sigma,1}^l$	3.18	2.52	25.4
$\infty_{\sigma,2}^l$	2.66	5.87	25.3
$\infty_{\sigma,3}^l$	5.78	2.62	25.3
$\infty_{m,1}^l$	0.82	4.78	25.2
$\infty_{m,2}^l$	4.21	1.26	25.4

2. Seeds from Grid Search

A grid search-based numerical approach offers a universal mechanism for seed generation, without restrictions on the types of admissible families. Although more computationally intensive than the asymptotic approach, its efficiency improves significantly when approximate regions of interest in the space are informed by prior knowledge of the optimality structure. The grid search is conducted on planar sections aligned with the selected optimality domains, as illustrated in Fig. 6. In the $M_1 - M_2$ domain, the search planes are parallel to the $M_1 - M_2$ plane (i.e., $t = c$ with a constant c , Fig. 6(a)). In the $T - t$ domain, the search planes are aligned with progressions in t , expressed

as $M_1/n_1 - M_2^{dep}/n_2 = c$ (Fig. 6(b)). Stationary points on these planes are identified using a numerical solver that enforces the first-order optimality conditions in the respective domains. In particular, for the temporal ($T - t$) domain, this procedure is analogous to a porkchop-based search for local minima; however, the objective here is to identify stationary points, forming a superset that includes minima, maxima, and saddle points. For the representative example depicted in Fig. 7, the porkchop plots are constructed over the ranges $0 \leq T \leq 2P_{syn}$ and $0.2P_2 \leq t \leq 2P_2$, where $P_{syn} = 2\pi/(n_2 - n_1)$ and $P_2 = 2\pi/n_2$. These bounds are selected to capture the dominant structures of the cost landscape for the illustrative case and do not represent a limitation of the proposed framework. In Fig. 7, the detected stationary points are marked according to the color scheme defined in Table 2 and serve as seeds for the subsequent continuation process.

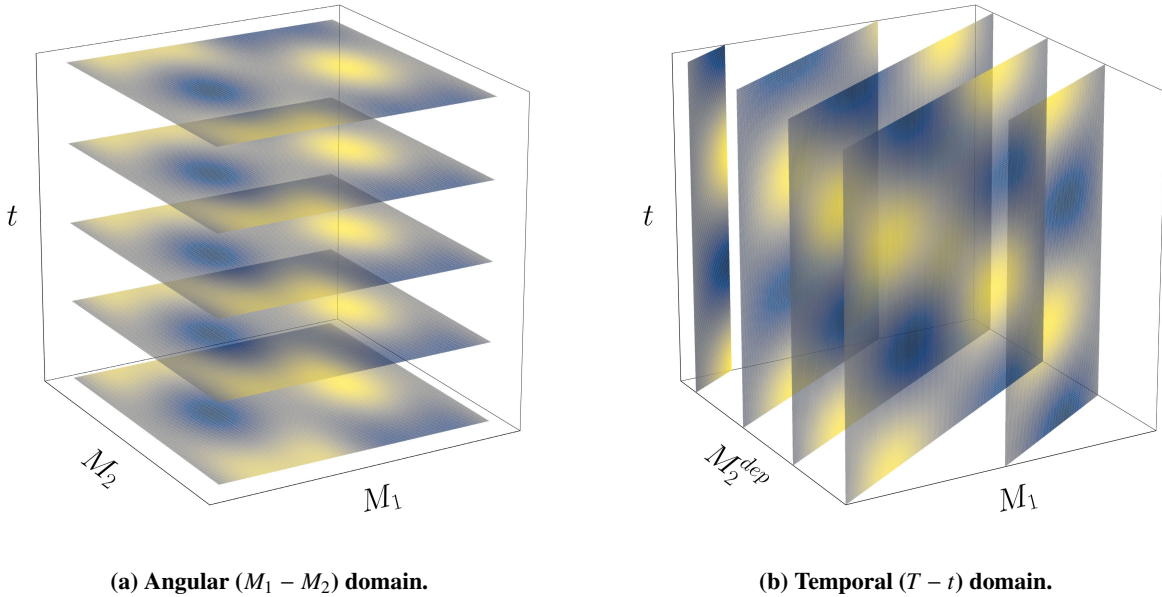


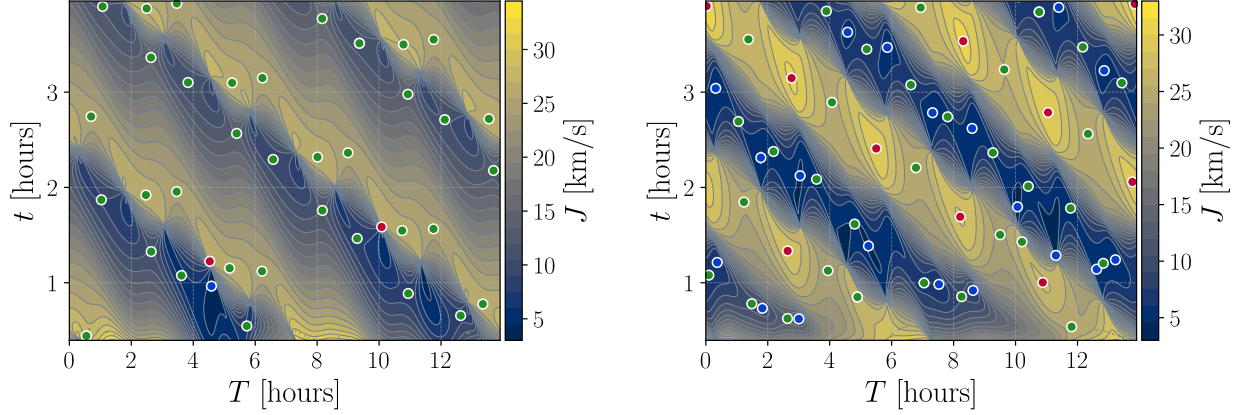
Fig. 6 Visualization of grid search strategies within the two optimality domains.

3. Other Seed Sources

In addition to asymptotic limits and grid-based searches, seeds may also be supplied using prior knowledge or diagnostic information obtained during the continuation process. For example, after completing continuation from all initially identified seeds, the absence of an expected connection between families may indicate missing branches. In such cases, additional seeds can be introduced to recover the complete family structure.

B. Family Continuation and End Points

Starting from the identified seeds, families of TIOTs are continued utilizing the numerical continuation scheme described in Section III.B. In this framework, one-parameter families are traced by enforcing two optimality conditions



(a) $d_1 = s$: 1 minimum, 2 maxima, and 37 saddle points. (b) $d_1 = l$: 19 minima, 10 maxima, and 34 saddle points.

Fig. 7 Identification of stationary points via grid search in the temporal domain.

while relaxing the remaining degree of freedom. From a given seed, continuation generally proceeds in two directions along the family. For convenience, any component of the state vector \mathbf{X} may be used to define the initial continuation direction; in the present study, the $\pm t$ directions are adopted. A suitable step size along the family is required to avoid unintended jumps between neighboring branches. Although the step size ds , from Eq. (19), is a user-defined parameter that may vary across applications, a value of $ds = 0.01$ is adopted for the case studies presented here^{††}, with the variables scaled as $(M_1, M_2, t/1000)$. From each seed, family members are generated sequentially in both directions until one of the following termination conditions (“end points”) is encountered:

1. Upper time-of-flight bound ($t > t_{max}$): Continuation is terminated when the time-of-flight exceeds a prescribed maximum threshold. In the present analysis, this value is set to $t_{max} = 40 \cdot 10^3$ seconds. Beyond this range, the transfer trajectories gradually approach the parabolic Lambert solutions associated with the asymptotic limit $t \rightarrow \infty$, and further continuation provides limited additional insight.
2. Lower time-of-flight bound ($t < t_{min}$): Continuation is also terminated when the time-of-flight drops below a minimum threshold, set to $t_{min} = 10$ seconds in this study. For shorter transfer times, the Lambert solutions typically become hyperbolic and exhibit increased sensitivity that destabilizes the continuation process and compromises numerical robustness.
3. Singularity at $\theta = 180^\circ$: A well-known singularity arises in the Lambert problem when the transfer angle satisfies $\theta = 180^\circ$. In this configuration, the orbital plane of the transfer arc becomes ambiguous, and the STM submatrix ϕ_{rv} , required to compute the sensitivities of the Lambert velocities with respect to the endpoint positions, becomes singular. For the reference case from orbits in Table 1, this singular configuration is illustrated in Fig. 8, where the red line denotes the nodal line that intersects both orbital planes. At $\theta = 180^\circ = \pi$ radians, two

^{††}Since ds measures arc length in a space of mixed units (radians for $M_{1,2}$ and a nondimensional time for $t/1000$), it does not carry a single physical unit; it serves purely as a scaling parameter that controls the step size within the free-variable (\mathbf{X}) space.

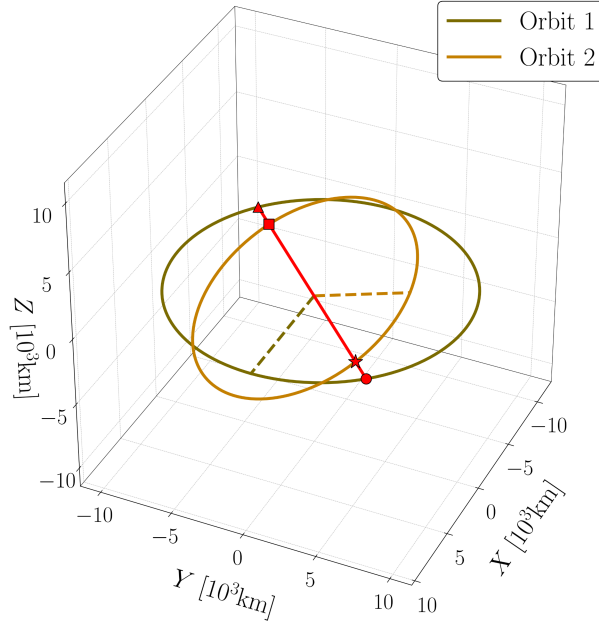


Fig. 8 Geometric configuration of the common nodal line (red): intersection of the departure and arrival orbital planes.

distinct geometric configurations are possible (Fig. 8): (1) $\bullet \rightarrow \blacksquare$, and (2) $\blacktriangle \rightarrow \star$. These configurations are denoted as π_1 and π_2 , respectively. In the temporal domain, two distinct empirical behaviors are observed in the vicinity of this singularity for the cases examined in this study. In some instances, two family branches appear to connect smoothly across $\theta = 180^\circ$. This singular configuration is associated with the transition between long- and short-transfer Lambert arcs. Several strategies may be adopted to handle this behavior within a continuation framework. Purely numerical approaches may increase the continuation step size to effectively “jump” across the singularity while switching the transfer-type indicator d_1 (long or short). More analytical or geometric treatments are also possible. For example, Sun [46] demonstrated that optimal transfer-plane orientations across $\theta = 180^\circ$ satisfy a Snell’s-law-like condition, a result later reproduced by Vinh et al. [5]. This suggests that the optimality constraints adopted here may transform into alternative geometric conditions at the singular configuration. In other instances, two distinct branches emerge that approach the singular configuration asymptotically as $t \rightarrow 0$, without exhibiting a smooth connection. A detailed analytical treatment of these behaviors near singularity, including a rigorous classification of the observed behaviors and their underlying causes, is beyond the scope of the present study. Nevertheless, empirical evidence indicates that smooth family continuation across $\theta = 180^\circ$ is possible in certain cases. Accordingly, the present work adopts a simple and robust strategy: continuation is halted as the solution approaches the singularity, and family connectivity across $\theta = 180^\circ$ is subsequently assessed *a posteriori* using porkchop-based seeds on the opposite side of the singularity. If a branch is found to be missing, an additional seed is supplied from the porkchop plot to recover the full family.

4. Completed cycle: For families that exhibit cyclic behavior, continuation is terminated when the current family member returns to the original seed. In the present investigation, such cyclic families are observed only in the temporal domain; the angular domain formulation does not yield closed-loop behavior for the cases examined. For the examples presented in this work, these four termination conditions encompass all observed family end points. Depending on the orbital geometry, additional behaviors may arise that violate the implicit assumptions of the current continuation scheme. For example, the Jacobian $\partial F/\partial X$ in Eq. (45) during the differential correction process may, in principle, admit a two-dimensional null space, indicating the intersection of multiple families at a single point. Although no such bifurcating configurations are observed in the present study, their potential existence motivates further investigation.

For the sample transfer scenario summarized in Table 1, families are generated from both asymptotic and grid search seeds. The resulting families are visualized in the three-dimensional $M_1 - M_2 - t$ space and are plotted in Figs. 9 and 10 for the asymptotic and grid search seeds, respectively. The families supplied from the grid search seeds fully encompass those generated from the asymptotic seeds. In contrast, cyclic families do not connect to the $t \rightarrow \infty$ asymptotes and therefore cannot be discovered leveraging asymptotic initialization alone. This observation highlights the complementary roles of the two seeding strategies within the proposed framework. In Figs. 9 and 10, two black dotted lines correspond to $\pi_{1,2}$, singular configurations defined from Fig. 8.

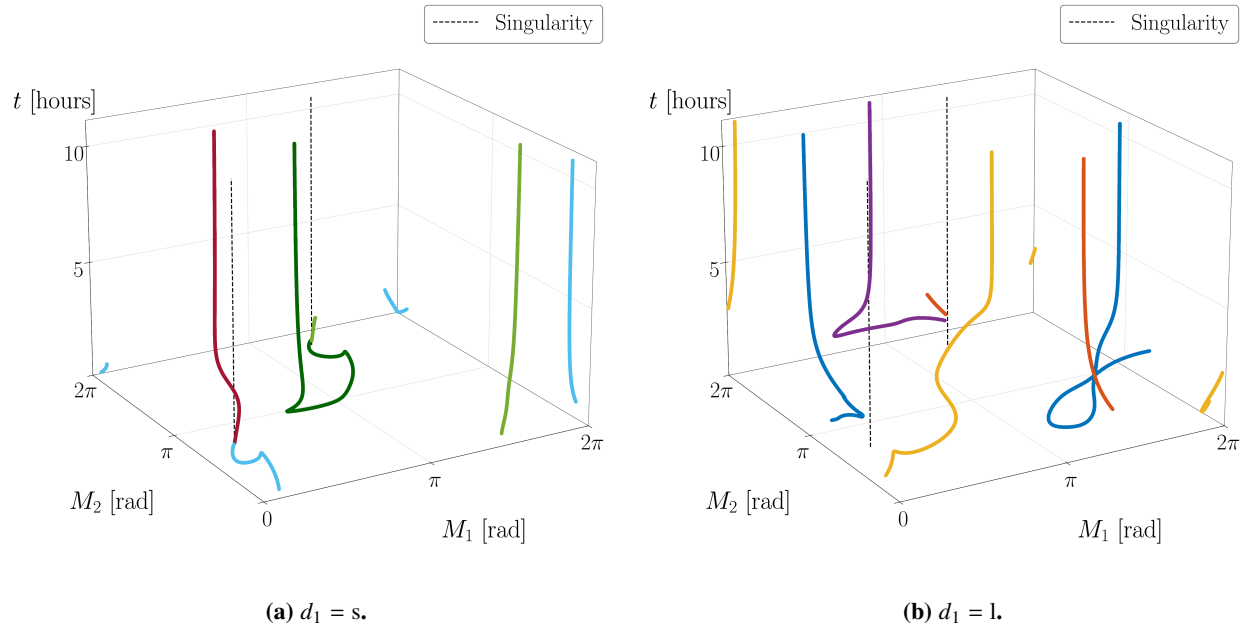


Fig. 9 Global structure of TIOT families initiated from asymptotic seeds (Table 4).

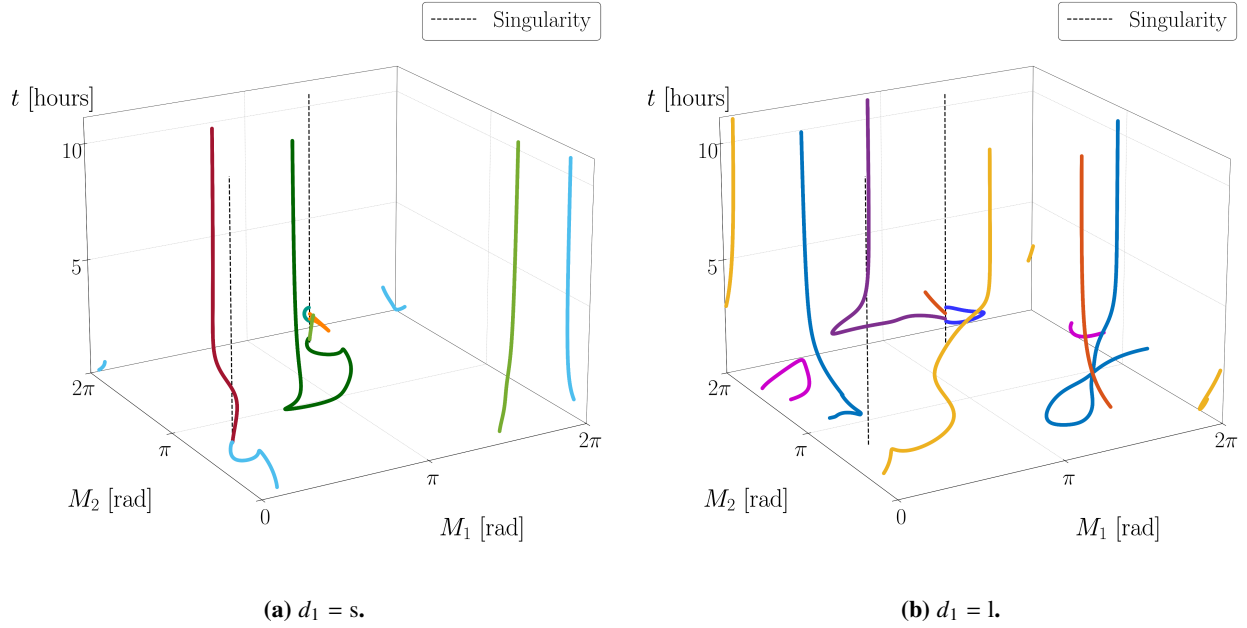


Fig. 10 Global structure of TIOT families initiated from grid search seeds (Fig. 7).

C. Solution Analysis

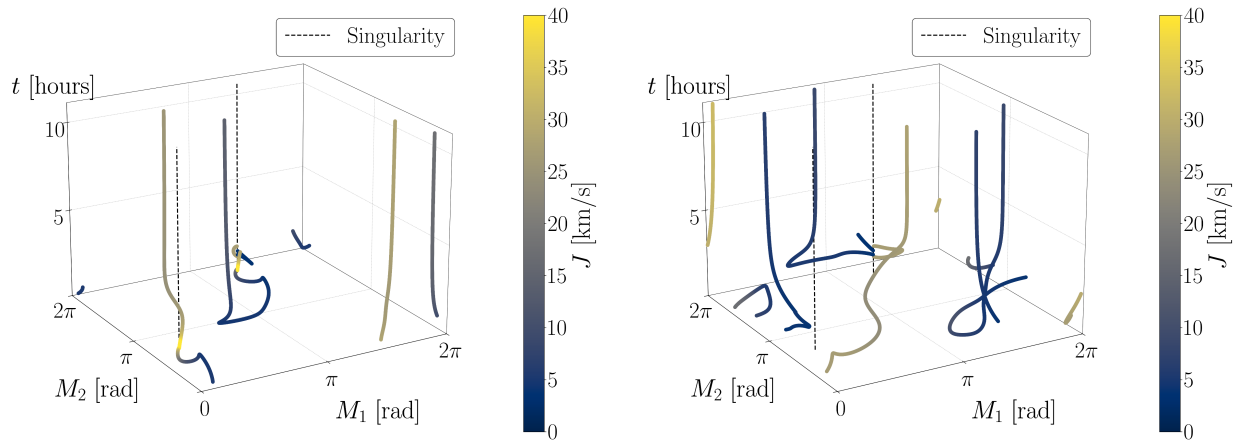
The families recorded during seed initialization and continuation are further analyzed to extract qualitative and quantitative insights into the structure of TIOT families. From this section onward, the analysis focuses on families generated from grid search seeds, as they supply the more comprehensive coverage of the solution space.

1. Total Cost J

The total transfer cost J is a primary quantity of interest. Figure 11 displays the families generated from grid search seeds, with the color indicating the magnitude of J . Lower-cost transfers naturally cluster along specific segments of the families, revealing geometries that are potentially attractive from a mission design perspective. To enhance visual discrimination among low-cost solutions, the color scale is restricted to the range $0 \leq J \leq 10$ km/s and re-plotted in Fig. 12. This adjusted scale highlights subtle cost variations within the most practically relevant subset of the solution space and clarifies the relative desirability of neighboring family branches.

2. Hessian

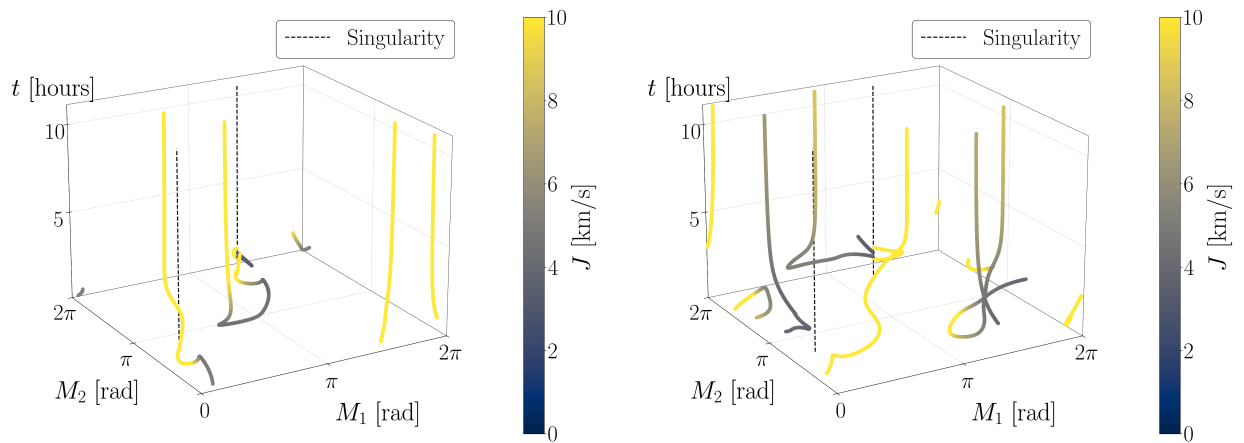
Although the continuation framework enforces first-order optimality conditions, the second-order optimality characteristics may vary along a given family. Accordingly, Hessian information is evaluated for all family members to distinguish between local minima, maxima, and saddle points. Figure 13 illustrates the families colored according to their Hessian classification (Table 2). A notable observation is that the optimality type may change continuously along a single family, indicating transitions between minima, saddles, and maxima without discontinuities in the underlying



(a) $d_1 = s$.

(b) $d_1 = 1$.

Fig. 11 Mapping of transfer cost J along the identified solution families.



(a) $d_1 = s$.

(b) $d_1 = 1$.

Fig. 12 Enhanced visualization of low-cost solution families ($0 \leq J \leq 10$ km/s).

transfer geometry. This behavior underscores the importance of treating families as continuous objects rather than collections of isolated optimal points.

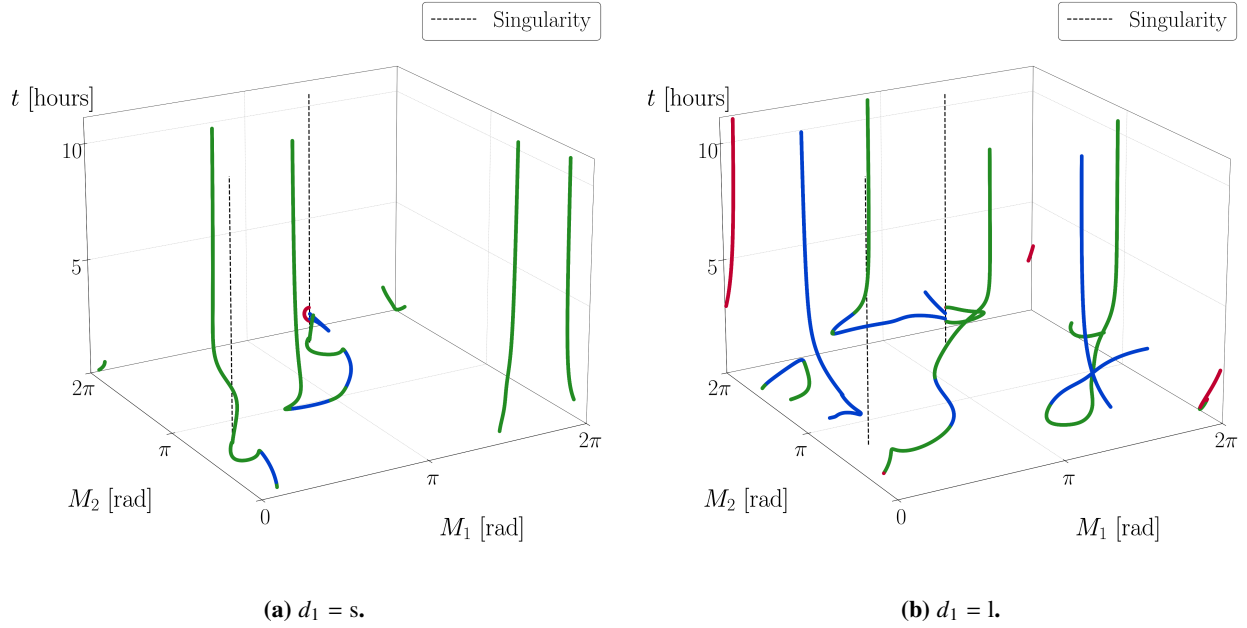


Fig. 13 Evolutionary transition of optimality types along the TIOT families. The colors represent the Hessian classification defined in Table 2 (blue: minimum, red: maximum, green: saddle point).

3. Assigning Family Index

Since different seeds may converge to different segments of the same continuous family, or, conversely, to distinct families that appear or disappear across the domain, a consistent family indexing scheme is required. Assigning indices to entire families enables a systematic characterization of the global solution structure, revealing the connections, evolutions, and terminations of families. This indexing facilitates consistent reference across figures and analyses and supports comparative studies of cost trends, optimality transitions, and geometric behavior, particularly in the presence of singular configurations where families may merge, split, or terminate. After removing duplicate segments obtained from different seeds, each unique family is assigned a distinct index. Figure 14 illustrates the 12 indexed families identified for the representative case, while Table 5 summarizes their end points and observed inter-family connections. The asymptotic end points at $t \rightarrow \infty$ are categorized following the labels from Table 4 and Eq. (25). Singular end points π_1 and π_2 correspond to the configurations $\bullet \rightarrow \blacksquare$ and $\blacktriangle \rightarrow \blackstar$ in Fig. 8, respectively. At the singular end points, families may either connect smoothly across the singularity or terminate asymptotically, depending on the local family geometry. A zoomed-in view in Fig. 14 highlights several examples where apparently distinct families merge into a unified structure when examined in the full parameter space (e.g., Families 2, 4, and 9, as well as Families 10 and 12). In contrast, other branches originate from the same singularity but do not connect in a smooth fashion (e.g., Families 6 and 7, as well as Families 5 and 8). While a rigorous analytical characterization of these singular connections is beyond the scope of the present study, the proposed indexing scheme provides a practical and unambiguous means of documenting the observed family connectivity and organizing the global solution structure.

Table 5 Summary of indexed TIOT families in the temporal domain for the baseline scenario (Table 1)

Family No.	End point 1	End point 2	Connections (if any)	Color
1	$\infty_{m,1}^1$	$\infty_{\sigma,3}^1$	-	
2	$\infty_{m,2}^1$	π_2	Family 9	
3	$\infty_{M,1}^1$	$\infty_{\sigma,1}^1$	-	
4	$\infty_{\sigma,2}^1$	π_2	Family 9	
5	$\infty_{\sigma,2}^s$	π_2	-	
6	$\infty_{\sigma,4}^s$	π_1	-	
7	$\infty_{\sigma,1}^s$	π_1	-	
8	$\infty_{\sigma,3}^s$	π_2	-	
9	π_2	π_2	Family 2, 4	
10	π_2	π_2	Family 12	
11	-	-	-	
12	π_2	π_2	Family 10	

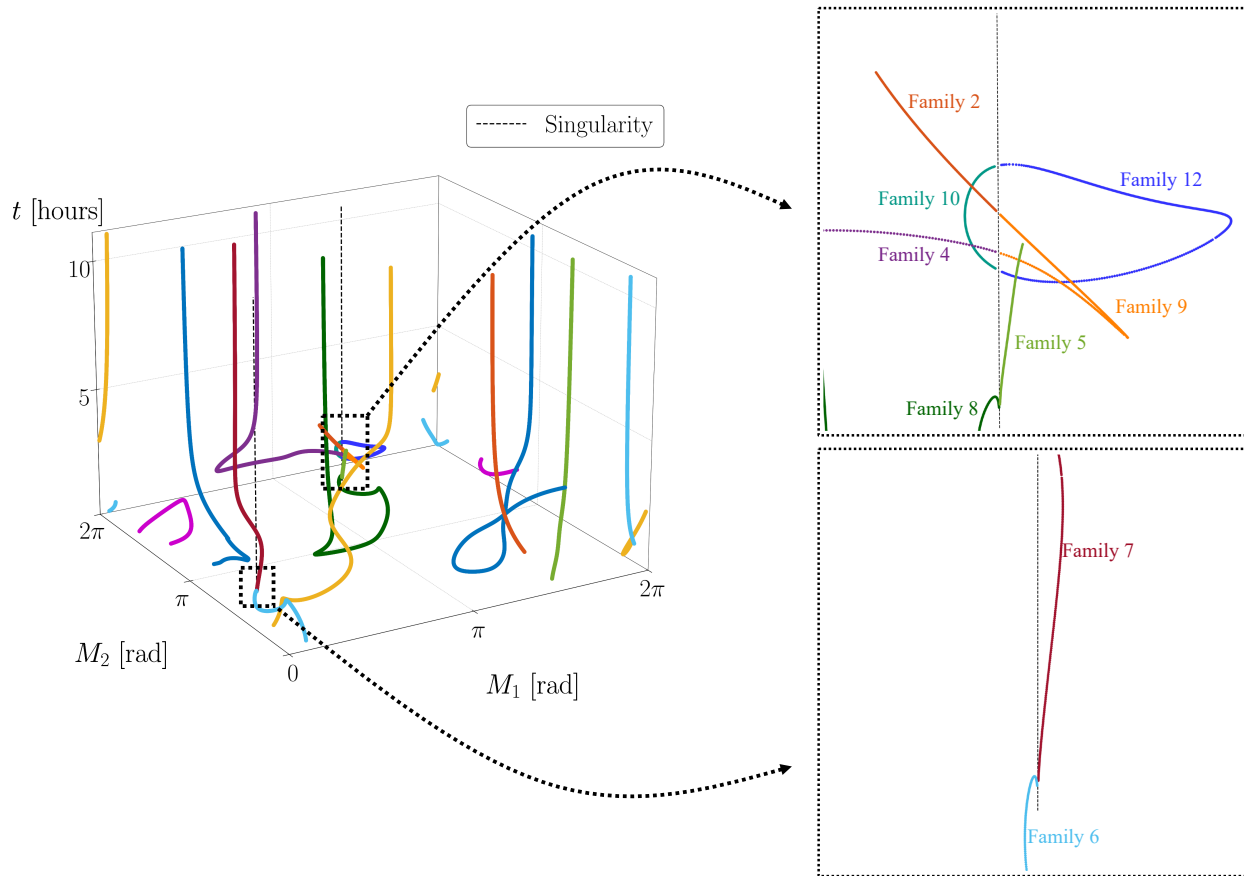


Fig. 14 Global structure of TIOT families in the temporal domain colored by their indices (Table 5).

4. PVT (Specific to the $T - t$ Domain)

Families generated by enforcing the temporal domain optimality constraints do not necessarily satisfy the necessary conditions from the PVT; as such, each TIOT is evaluated for the PVT conditions. For a given transfer, the primer vector is reconstructed by solving a two-point boundary value problem, ensuring alignment of the primer vector with the impulsive velocity changes at both burn locations, i.e., $\mathbf{p}_j = \Delta \mathbf{v}_j / |\Delta \mathbf{v}_j|$ for $j = 1, 2$. The resulting primer vector history is then checked against the remaining PVT conditions. Under the assumption of two impulsive burns and smooth dynamics, the key requirement is that the magnitude of the primer vector remains strictly less than unity along the interior of the transfer arc. Violation of this condition implies that an additional intermediate burn is required for local optimality. Figure 15 displays the families colored according to both their Hessian classification and PVT satisfaction. Family members that do not satisfy the PVT requirements are plotted in gray. Family members that satisfy the PVT criteria are colored with the scheme following Table 2. Note, as PVT supplies necessary conditions, it is possible that local maxima and saddle solutions (red and green in Fig. 15, respectively) also satisfy the PVT criteria.

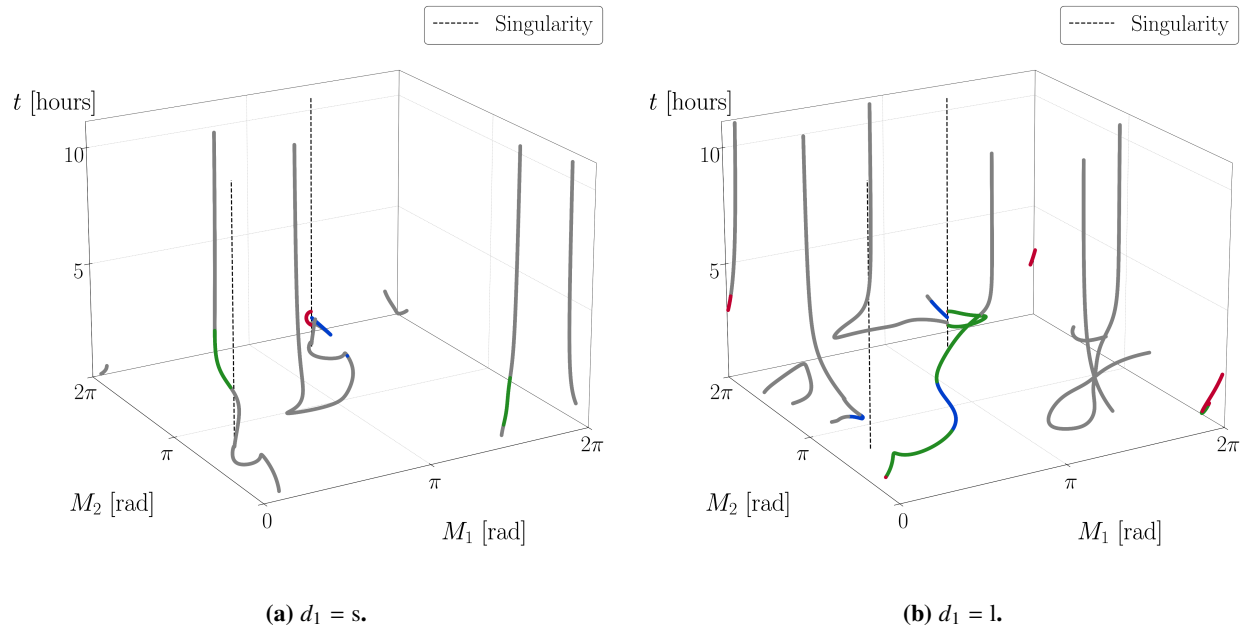


Fig. 15 Validation of impulsive optimality utilizing the PVT criteria along the solution families. The color scheme follows Table 2, while segments that violate PVT necessary conditions are marked in gray.

5. Projection to Porkchop Plots (Specific to the $T - t$ Domain)

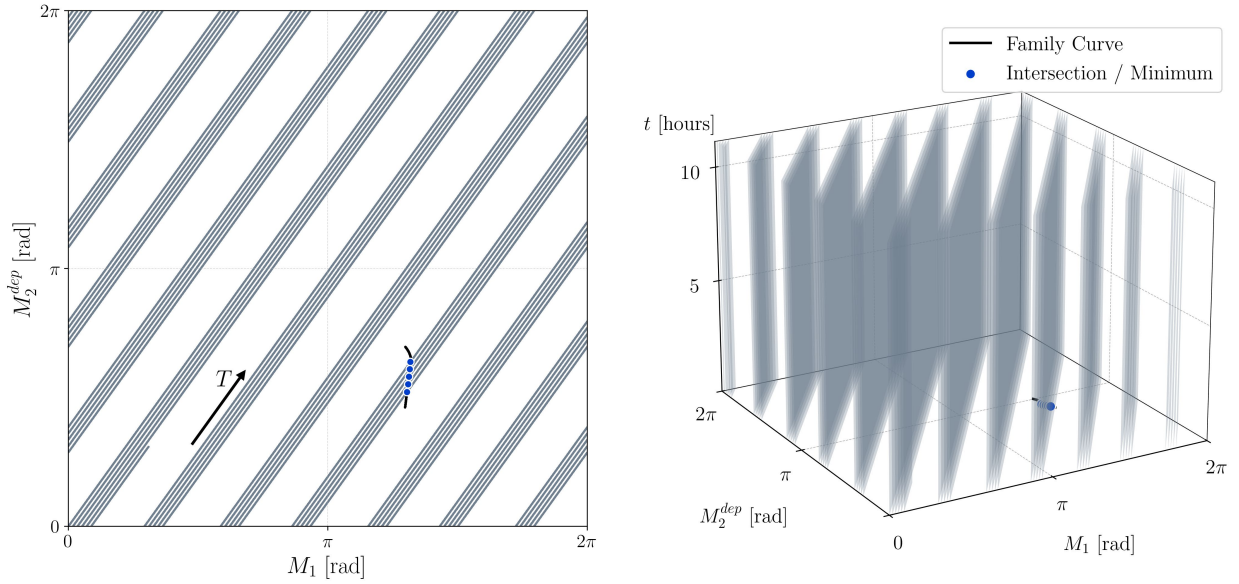
Families of TIOTs provide a compact, global representation of solutions that would otherwise require exhaustive searches over large time windows. To connect this family-based perspective with conventional porkchop plots, family members are projected onto the $T - t$ domain. The key idea is to reinterpret the “time axis” of a porkchop plot through the evolution of the angular variables. As time T progresses, the angles advance linearly, so that $M_1 = n_1 T + M_1^0$,

$M_2^{dep} = n_2 T + M_2^0$, tracing straight “time-lines” in the $M_1 - M_2^{dep}$ domain^{‡‡}. In practice, these time-lines may be visualized as black straight trajectories in Fig. 16(a) initiating from $M_1^0 = M_2^0 = 0$. After one full revolution in either angle, the corresponding angle wraps around and the trajectory re-initializes from 0 in that angular coordinate. When the mean motion ratio n_1/n_2 is non-resonant, the time-lines become dense over an infinite time span: as $T \rightarrow \infty$, it visits arbitrarily close to every possible combination of $M_1 - M_2^{dep}$. In this sense, the base variable of a porkchop plot, T , is decomposed into the angular variables that parametrize the family curves in $M_1 - M_2^{dep} - t$ space, tracing the time-lines or “time-planes” in Figs. 16(a) and 16(b), respectively. With this interpretation, stationary points on porkchop plots arise naturally as intersection events. Specifically, intersections between the time-lines (or, time-planes) and an TIOT family curve correspond to transfer configurations that satisfy the stationary conditions in the $T - t$ domain. Figure 16 illustrates this process for a local minimum fragment satisfying PVT of one representative family (e.g., Family 9 in Table 5); the family is illustrated in the $M_1 - M_2^{dep} - T$ space together with the time-planes (Fig. 16(b)), and the intersection points map directly to stationary points in the porkchop plot (Fig. 16(c)). In this case, the intersecting members are locally minimum TIOTs and, thus, colored in blue. Repeating this process over all indexed families yields a systematic catalog of stationary points across the porkchop domain, as illustrated in Fig. 17. The white dotted box corresponds to the initial bounds for the grid search supplying initial seeds within the framework (Section V.A.2). This projection-based approach complements conventional porkchop analysis. One may certainly inspect porkchop plots visually and/or apply gradient-based solvers to locate local extrema [16]. However, porkchop plots are fundamentally constrained by grid resolution: when multiple extrema are closely spaced or visually indistinguishable, reliable detection typically requires a finer grid and additional numerical effort. Moreover, when the time window of interest is wide, a large fraction of the sampling effort becomes wasteful because only limited regions contain meaningful optima. Although periodicity can sometimes be exploited to reduce the search domain [16], the Lambert geometry is not perfectly repetitive, and optima may appear or disappear between cycles. Without global structural insight, one may either miss relevant solutions or expend substantial computation exploring uninformative regions. In contrast, the proposed framework replaces repeated local optimization over time windows with the identification of intersection points between two curves, i.e, the time-lines and TIOT families. Once the families are computed, the time-line construction applies to an effectively unbounded range of T under the assumed Keplerian dynamics, enabling efficient and systematic detection of stationary points without relying on high-resolution porkchop sampling.

VI. Case Studies

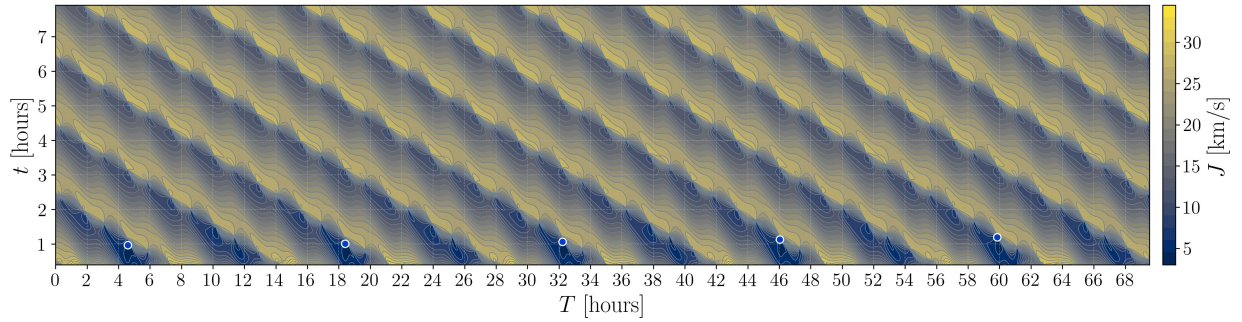
This section demonstrates the proposed framework through a set of representative transfer scenarios. First, a baseline scenario is established that coincides with the illustrative example utilized in the preceding sections (Table 1). This case

^{‡‡}While the results thus far primarily visualize families in the $M_1 - M_2$ domain, the $M_1 - M_2^{dep}$ domain is more effective for juxtaposing the $T - t$ porkchop representation with the higher-dimensional family structure.



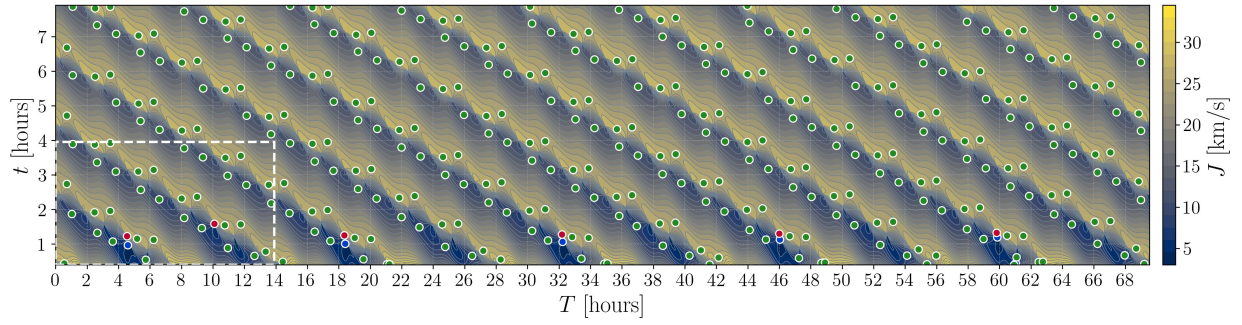
(a) Two-dimensional view ($M_1 - M_2^{dep}$ domain).

(b) Three-dimensional view ($M_1 - M_2^{dep} - t$ domain).

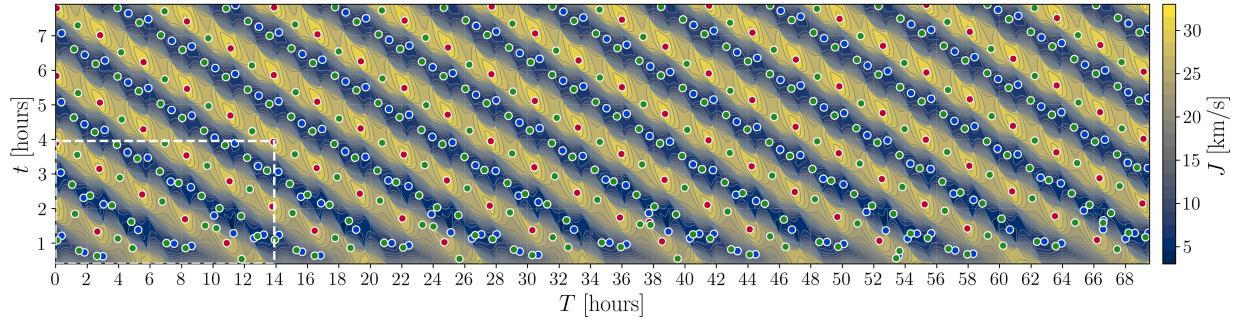


(c) TIOTs mapped onto a porkchop plot.

Fig. 16 Projection and intersection of Family 9 (Table 5 and Fig. 14) with a representative porkchop plot.



(a) $d_1 = s$.



(b) $d_1 = 1$.

Fig. 17 Projection of all TIOT families (Table 5 and Fig. 14) onto a porkchop plot. The white dashed box indicates the limited range of the initial grid search used for seed generation (Fig. 7).

is examined in detail to provide a comprehensive “atlas” of TIOT families, including representative transfer geometries and a classification of family branches. Within this baseline landscape, particular attention is paid to practically desirable configurations, specifically, locally minimal solutions that also satisfy the PVT necessary conditions for two-impulse optimality. The burn characteristics and transfer orbit properties of these desirable configurations are analyzed to provide physical insight. Second, a controlled parametric study is conducted by varying the relative inclination while holding the remaining orbital elements fixed to the baseline configuration. This study tracks the evolution of the desirable configurations and their associated families as the inclination increases, revealing bifurcations as well as the creation or disappearance of solution branches. Finally, the broader implications and limitations of the current results are discussed, highlighting the role of the family-based viewpoint in complementing conventional porkchop-based searches.

A. Baseline Transfer Scenario (Table 1)

1. Global Landscape and Family Classification

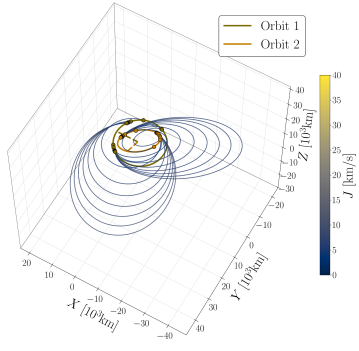
Within the temporal domain, 12 families are identified and indexed in Table 5, as plotted in Fig. 14. Representative transfer geometries for each TIOT family are depicted in Fig. 18. Each family yields unique intersections on the porkchop plot, where detailed behaviors are recorded in Appendix F. Naturally, not all solution geometries are of practical utility; solutions with undesirable characteristics, such as an excessively large J , may be screened out.

2. Anatomy of Min- J Geometries

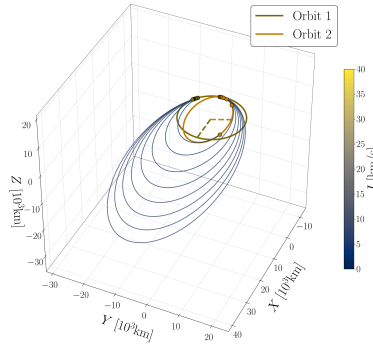
Among the various locally stationary families, those that contain local minima satisfying the PVT conditions are examined further. While all members along a given family are locally stationary, the member achieving the minimum cost J within the family is termed the “min- J ” TIOT. Figures 19–21 illustrate three such configurations^{§§}. Figures 19(a), 20(a), and 21(a) display the family branches in the solution space. The first optimal configuration spans across Families 2 and 9; thus, these two families are presented together in Fig. 19(a). Additionally, the min- J TIOT in each configuration is depicted in the Earth-centered inertial frame in Figs. 19(b), 20(b), and 21(b).

The first two geometries (Figs. 19–20) share common characteristics. These transfers typically occur in the vicinity of the nodes, i.e., both the departure and arrival points lie near the common nodal line where the two orbital planes intersect. This configuration is also observable from the locations of the optimal members within the $M_1 - M_2$ domain that lie close to the singular lines, π_1 and π_2 . However, as noted by Vinh et al. [5], exact nodal transfers ($\theta = 180^\circ$) typically do not render locally optimal solutions. For the specific orbital combination in Table 1, the departure orbit is associated with a larger radius from the central body (Earth). Consequently, the optimal transfers utilize a departure burn that primarily corrects for the inclination change. Table 6 details the burn characteristics for the min- J configurations. The components of the two burns, $|\Delta v_1|$ and $|\Delta v_2|$, are decomposed into the unit vectors of the Local Vertical Local

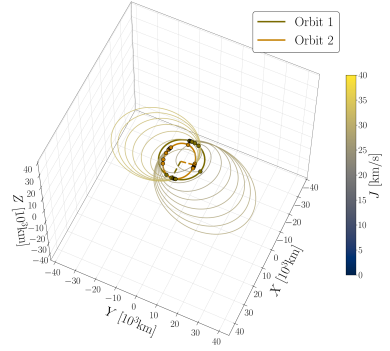
^{§§}While Family 3 also supplies members with locally minimal TIOTs that satisfy the PVT conditions, they represent hyperbolic Lambert arcs and are not considered desirable.



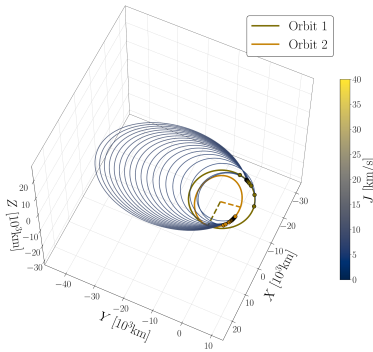
(a) Family 1.



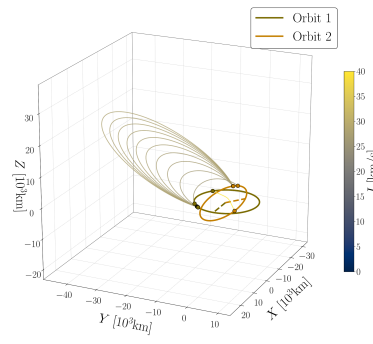
(b) Family 2.



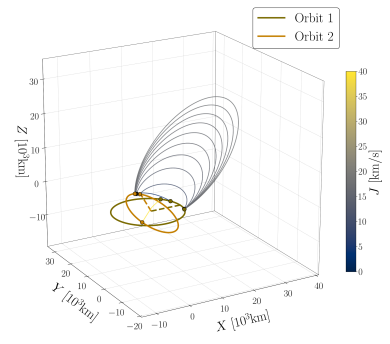
(c) Family 3.



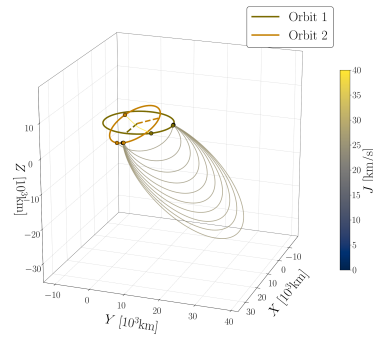
(d) Family 4.



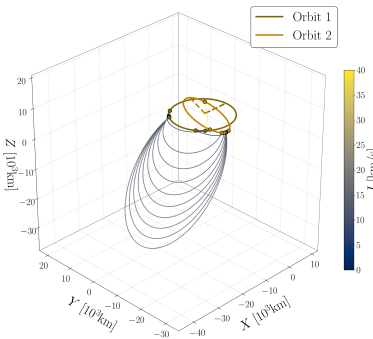
(e) Family 5.



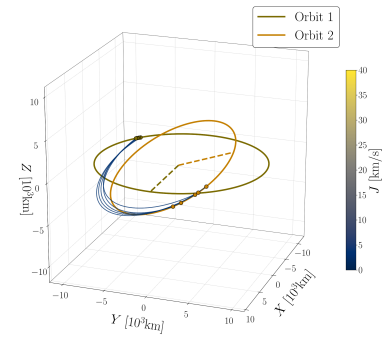
(f) Family 6.



(g) Family 7.



(h) Family 8.



(i) Family 9.

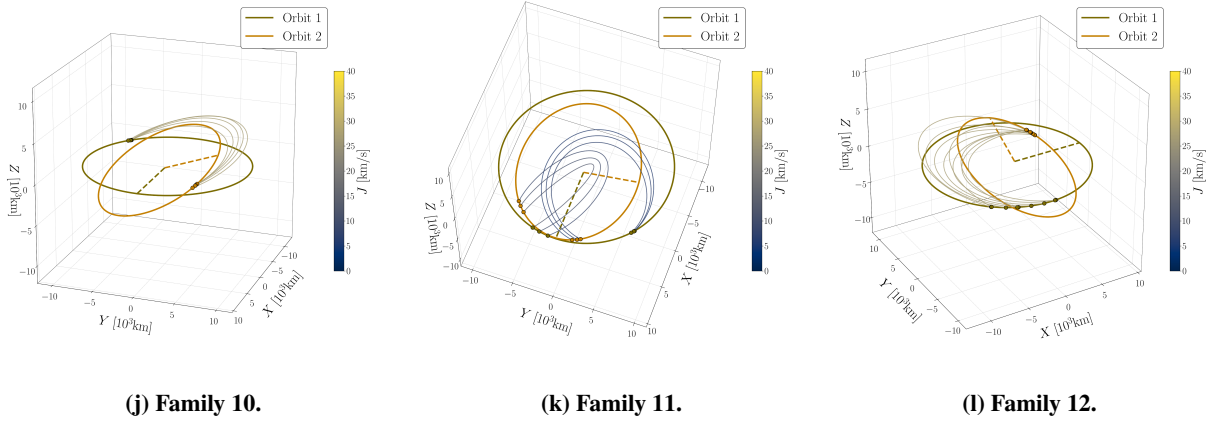


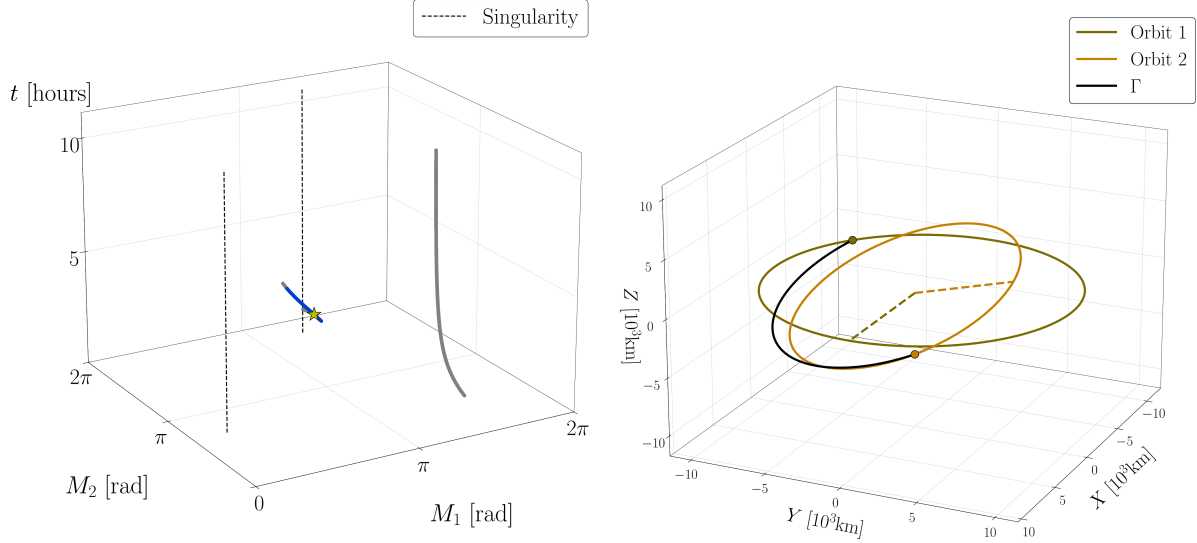
Fig. 18 Visual catalog of the 12 identified TIOT families (Fig. 14) for the baseline scenario (Table 5).

Horizontal (LVLH) frame: the radial unit vector \hat{r} , the angular momentum direction \hat{h} , and the tangential direction \hat{t} . Burns in the \hat{h} -direction are responsible for changing the orbital plane (i, Ω). A key distinction regarding the plane change strategy is observed between the first two configurations. Note that the departure and arrival orbits are inclined at $i_1 = 0$ and $i_2 = 30^\circ$, respectively. Min- J TIOT 1 performs nearly all necessary inclination change at departure ($|\Delta v_h| \approx 2.58$ km/s), resulting in a transfer orbit inclination of $i \approx 27.6^\circ$, close to the target's 30° . In contrast, min- J TIOT 2, departing near the perigee, distributes the plane change maneuver more evenly; it reaches an intermediate inclination of only $i \approx 20.8^\circ$, leaving a significant correction ($|\Delta v_h| \approx 0.79$ km/s) for the arrival burn. This difference substantiates the underlying asymmetry between the two configurations. Given the non-circular geometry of the orbits ($e_1 = e_2 = 0.1$), the two configurations offer distinct transfer opportunities. Since the first geometry permits a departure near the apogee ($M_1 \approx 180^\circ$) and an arrival near the perigee ($M_2 \approx 0^\circ$), the optimal solution favors a larger inclination change at the first burn where the velocity is lower. In contrast, the second geometry is associated with a departure near the perigee ($M_1 \approx 0^\circ$) and an arrival near the apogee ($M_2 \approx 180^\circ$), rendering the inclination change at the first burn less efficient.

The third min- J TIOT presents an intriguing case that contrasts with the previous examples. While the first two min- J configurations naturally align with the expected geometries near the nodes, the third solution emerges as an additional, distinct local optimum. Although it bears a superficial resemblance to the first TIOT, it originates from a completely separate family branch, as evidenced by the disconnection between Families 8 and 9 in Fig. 14. Notably, this transfer exhibits the highest cost, driven by a massive initial plane change ($|\Delta v_h| \approx 2.93$ km/s) that instantly matches the target inclination ($i \approx 30.2^\circ$). The appearance of this isolated optimal branch, existing independently from the primary nodal families, highlights the non-trivial topology of the solution space. While this analysis cannot be generalized to other orbital configurations, it supplies useful insights into transfers with non-negligible inclination change ($\Delta i = 30^\circ$).

By combining the identified optimal families and members, it is possible to visualize the options within the

$M_1 - M_2^{dep}$ domain, as depicted in Fig. 22. The intersections of the time-line and the optimal families (here, only the local minima satisfying the PVT conditions are plotted) indicate the availability of the optimal geometry as a function of T . This information is valuable for mission planning, specifically for determining the required wait time (T) to access a desirable configuration. Ultimately, this visual representation underscores the distinct advantage of the proposed family-based framework. By tracing the continuous loci of local optima, the method supplies a comprehensive exploration of the solution space.



(a) Families 2 and 9 in the $M_1 - M_2 - t$ space. The color scheme is identical to Fig. 15.

(b) Min- J TIOT 1 (yellow star in Fig. 19(a)).

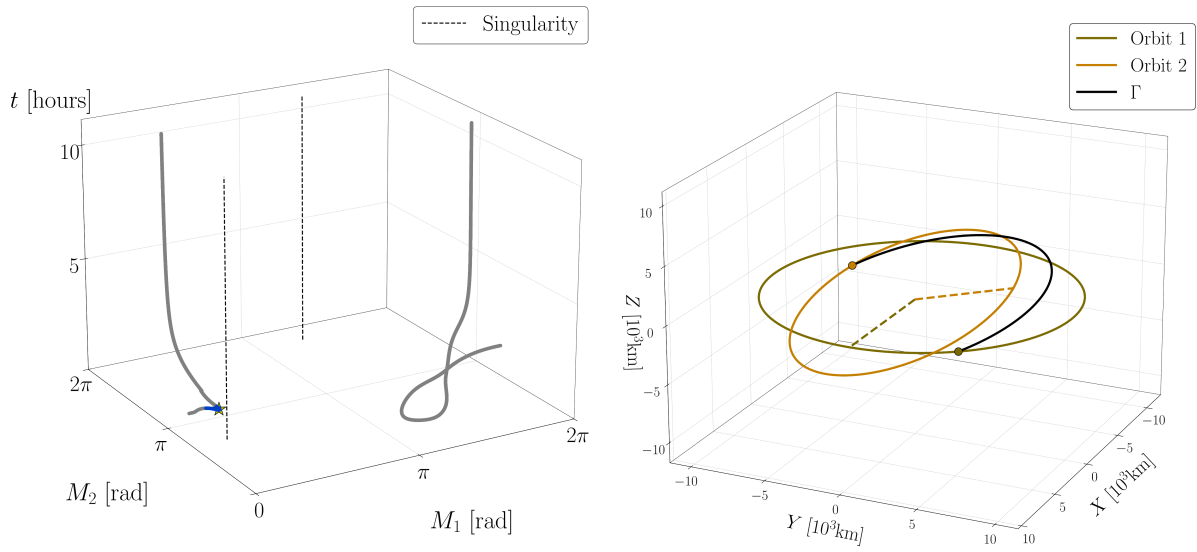
Fig. 19 Candidate optimal configuration 1 located in Families 2 and 9.

Table 6 Detailed burn characteristics and impulse components for the three min- J configurations (Figs. 19–21)

	Min- J TIOT 1 (Fig. 19(b))		Min- J TIOT 2 (Fig. 20(b))		Min- J TIOT 3 (Fig. 21(b))	
	Burn 1	Burn 2	Burn 1	Burn 2	Burn 1	Burn 2
Total J [km/s]	3.34		3.67		3.86	
$ \Delta \mathbf{v} $ [km/s]	2.83	0.52	2.49	1.18	3.09	0.77
$ \Delta \mathbf{v}_r $ [km/s]	0.78	0.26	0.63	0.54	0.67	0.51
$ \Delta \mathbf{v}_t $ [km/s]	0.84	0.40	0.72	0.70	0.70	0.50
$ \Delta \mathbf{v}_h $ [km/s]	2.58	0.21	2.30	0.77	2.93	0.28

B. Parametric Study: Topological Evolution under Inclination

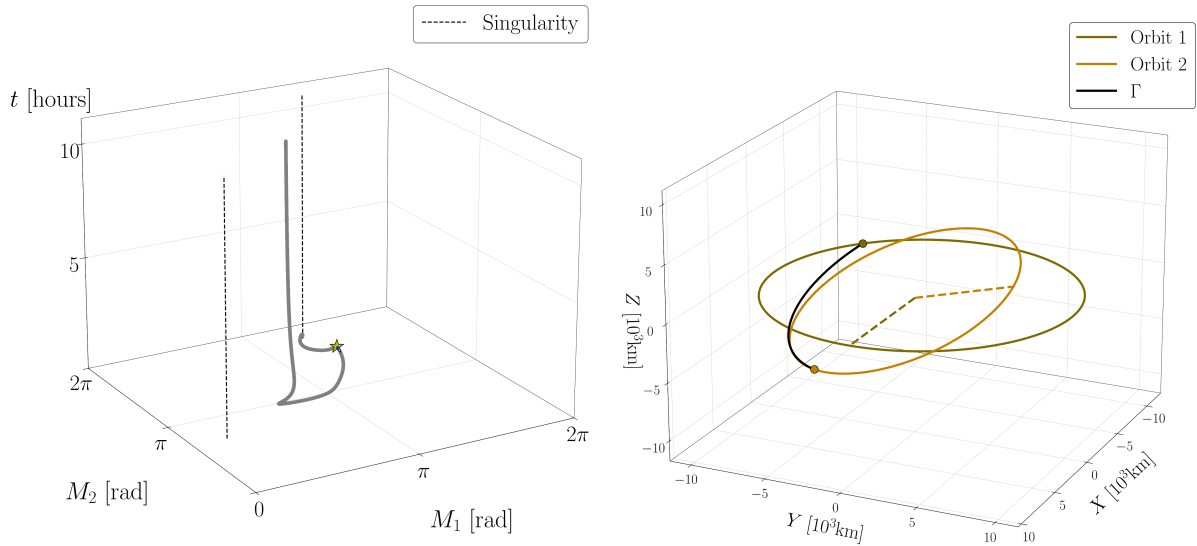
The generalized orbital transfer problem involves a high-dimensional parameter space governed by the orbital elements of the departure and arrival orbits. While the proposed framework is fully capable of exploring variations



(a) Family 1 in the $M_1 - M_2 - t$ space. The color scheme is identical to Fig. 15.

(b) Min- J TIOT 2 (yellow star in Fig. 20(a)).

Fig. 20 Candidate optimal configuration 2 located in Family 1.



(a) Family 8 in the $M_1 - M_2 - t$ space. The color scheme is identical to Fig. 15.

(b) Min- J TIOT 3 (yellow star in Fig. 21(a)).

Fig. 21 Candidate optimal configuration 3 located in Family 8.

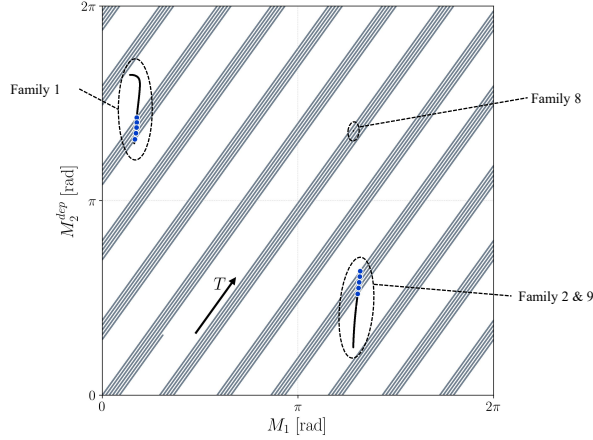


Fig. 22 Mission planning through crossings between the time-lines and families of TIOTs.

across all these dimensions, attempting to analyze simultaneous variations would obscure the fundamental mechanisms driving the solution topology. Therefore, this study adopts a controlled parametric approach to isolate the impact of the plane change requirement as an exemplary analysis. While fixing other orbital parameters in Table 1, multiple values for inclination are examined on the arrival side. A total of 15 cases are examined, tracking the families from $i_2 = 0^\circ$ to 10° with 1° incremental steps, followed by larger intervals at $i_2 = 15^\circ, 20^\circ, 25^\circ, 30^\circ$. Special attention is directed toward the emergence and deformation of the practically desirable configurations identified previously with increasing inclination gap. By assessing the topology at incremental levels of inclination, it is possible to identify critical transitions, such as bifurcations, reconfigurations, or the disappearance of solution branches, that connect the familiar coplanar solutions to the complex structures observed for the baseline scenario discussed in Section VI.A.2.

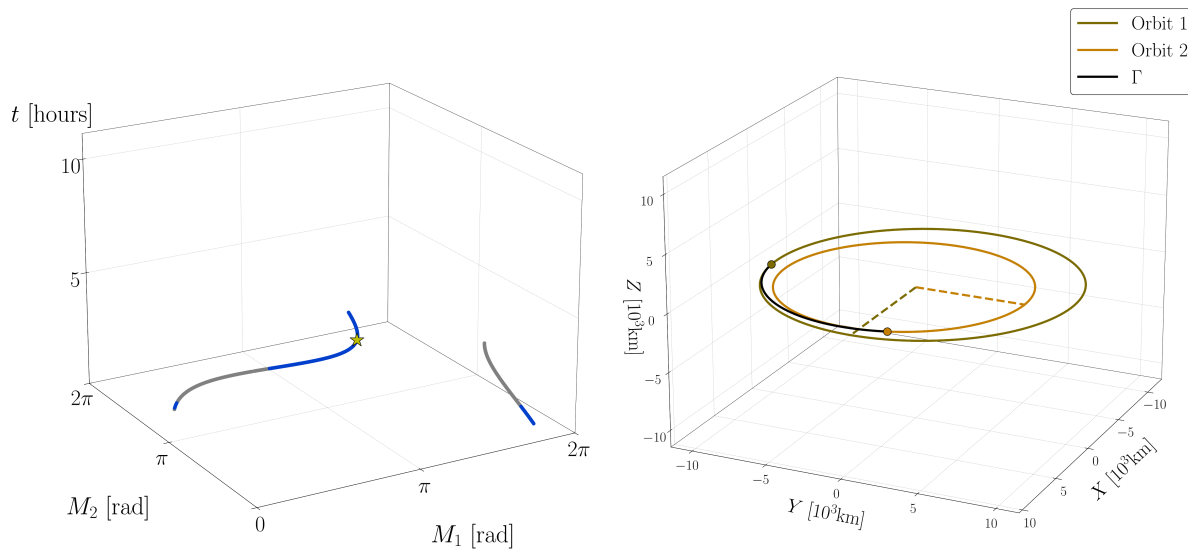
1. Coplanar Case ($i_2 = 0^\circ$)

The three desirable configurations identified in the preceding section (Figs 19-21) originate from two distinct family branches in the coplanar transfer scenario. Denoting these families as “root” families, their behaviors in the three-dimensional solution space and the respective $\min\text{-}J^{\text{min}}$ TIOTs along each family are supplied in Fig. 23. Note that Root family 1 (Fig. 23(a)) displays a closed-loop behavior, hosting a wide range of TIOT solutions that are locally minimal and simultaneously satisfy the PVT requirements. In contrast, Root family 2 (Fig. 23(c)) originates from asymptotes at $t \rightarrow \infty$ and notably, contains no member that satisfies the PVT necessary conditions while being locally minimal.

2. Bifurcation between $i_2 = 0^\circ$ and $i_2 = 1^\circ$

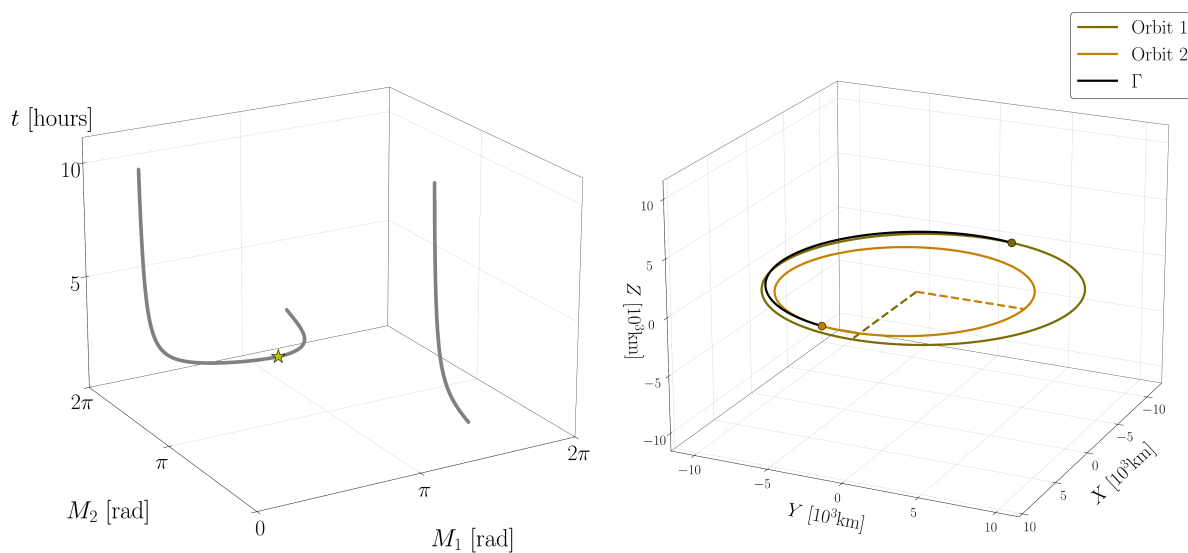
A non-zero inclination fundamentally alters the admissible geometries and branch structure of the TIOT families. Figure 24 illustrates the evolution of the root families as i_2 increases from 0° to 1° . The emergence of a singular line

^{min}As defined in Section VI.A.2, the “min- J ” TIOT denotes the member achieving the minimum cost J within the family.



(a) Root family 1. The color scheme is identical to Fig. 15.

(b) Min- J TIOT along the family.



(c) Root family 2.

(d) Min- J TIOT along the family.

Fig. 23 Behaviors of “root” families in the coplanar transfer scenario.

introduces a pathway linking to Root family 1. While this family forms a closed loop in the coplanar case, the inclined configuration leads to a merging behavior near the singular configuration π_1 . The resulting branch no longer closes, but instead exhibits asymptotic behavior, with its two ends approaching $t \rightarrow \infty$ and $t \rightarrow 0$, respectively, while remaining close to π_1 . This topological transition reflects a bifurcation in the family structure triggered by the introduction of a small but non-zero inclination. Additionally, the introduction of a non-zero inclination results in a noticeable shrinkage in the subset of family members that satisfy the PVT conditions (compare Figs. 23(a) and 24(a)). For Root family 2, the positive inclination enables the emergence of an optimal configuration that satisfies the PVT condition, a behavior not observed in the coplanar case (see Fig. 23(c)). Although this family evolves along a trajectory distinct from the coplanar case, its asymptotic behavior and the locations of its asymptotes remain nearly unchanged, indicating that the global structure of the family is preserved while its local optimality properties are modified.

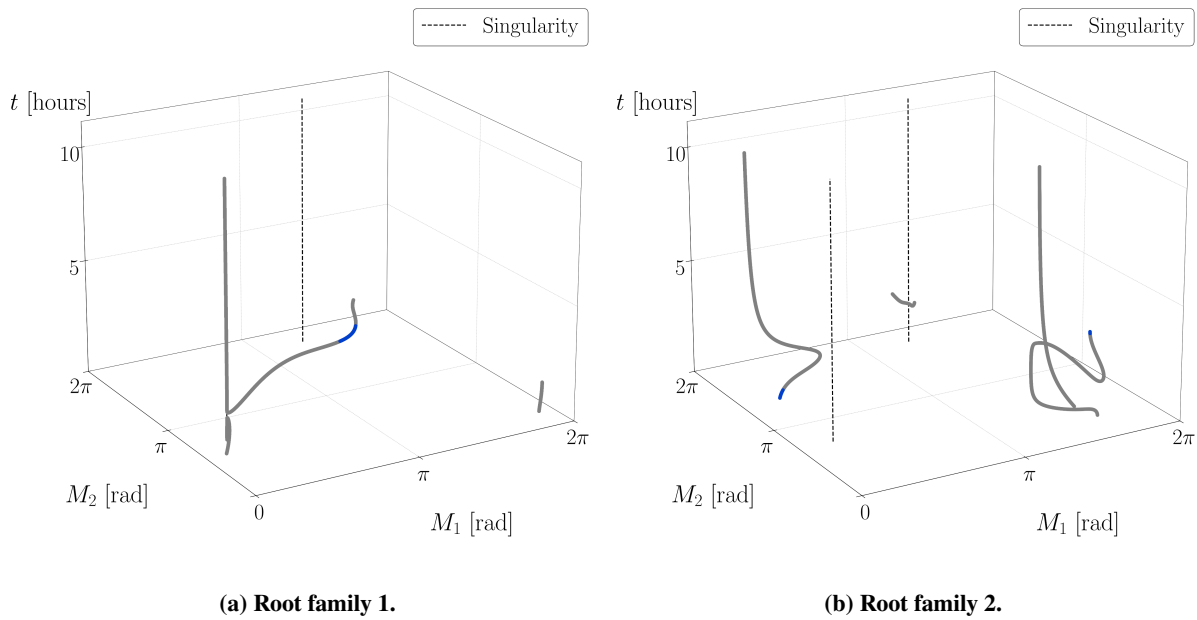
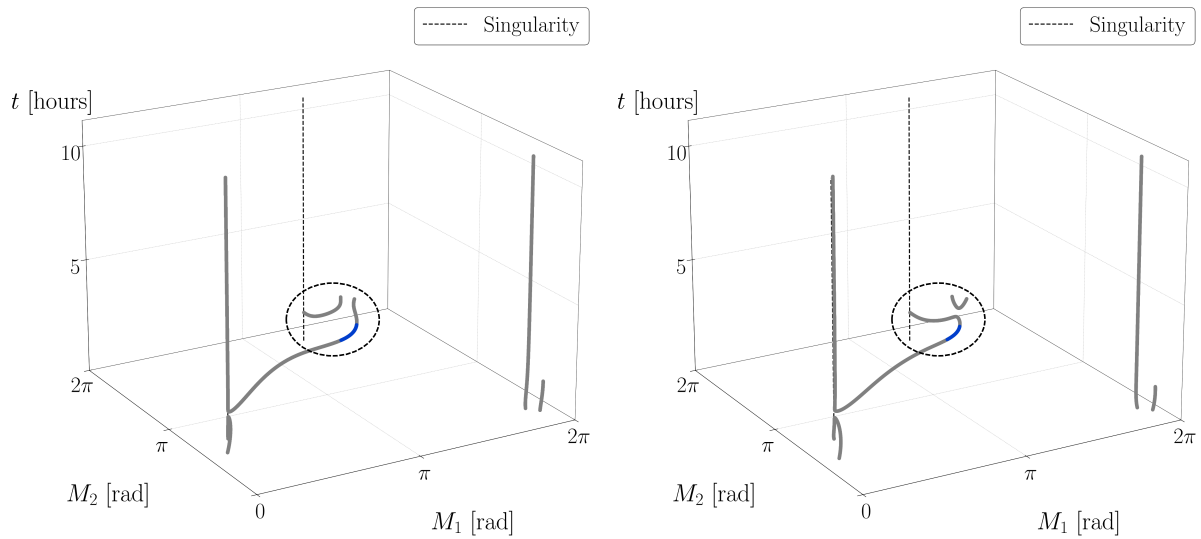


Fig. 24 Structural bifurcation induced at $i_2 = 1^\circ$.

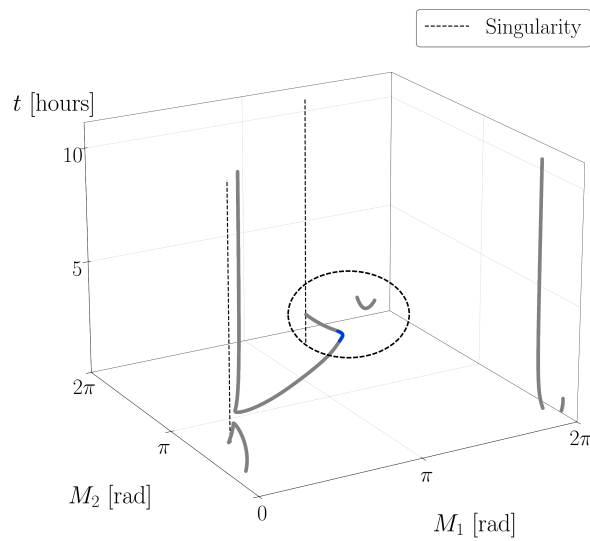
3. Bifurcation between $i_2 = 1^\circ$ and $i_2 = 2^\circ$

The first root family undergoes a subsequent bifurcation between $i_2 = 1^\circ$ and $i_2 = 2^\circ$. At $i_2 = 1^\circ$, a nearby branch exists that originates from the singular line π_2 and traverses in the vicinity of Root family 1. As i_2 increases, a change in connectivity occurs; Root family 1 turns and connects to the singular line. After this reconfiguration, the two branches drift further apart as the inclination increases (Fig. 25(c)).



(a) Root family 1 at $i_2 = 1^\circ$ and a nearby branch.

(b) Root family 1 at $i_2 = 2^\circ$ and a reconfiguration.



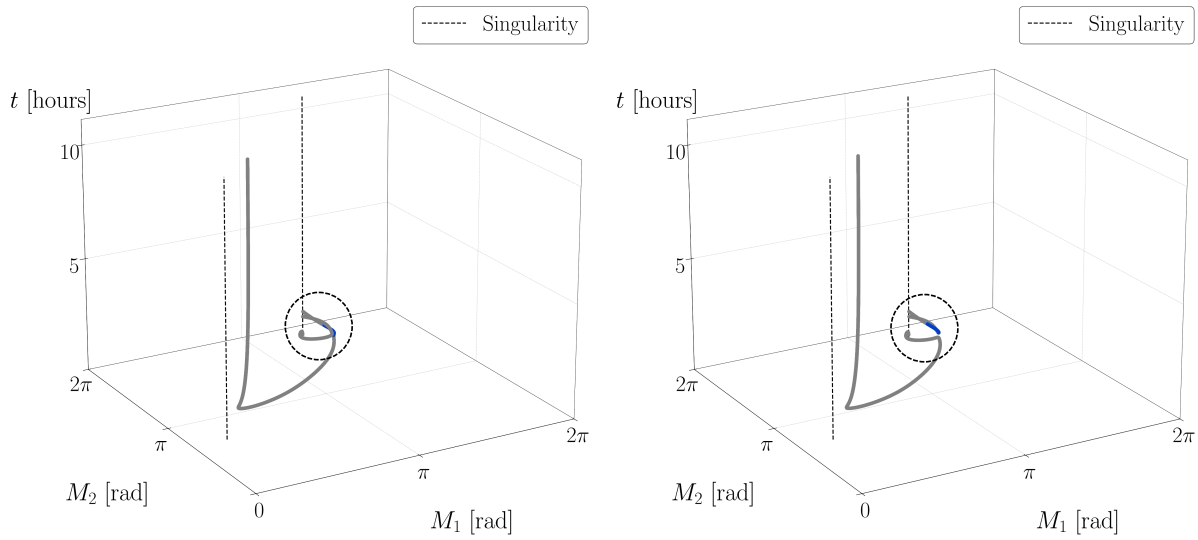
(c) Root family 1 at $i_2 = 5^\circ$ with a progressive drift.

Fig. 25 Bifurcation of Root family 1 between $i_2 = 1^\circ$ and $i_2 = 5^\circ$.

4. Bifurcation between $i_2 = 8^\circ$ and 9°

Another significant bifurcation occurs between $i_2 = 8^\circ$ and 9° . In this regime, a branch with endpoints at $\theta \rightarrow 180^\circ$ traverses close to the Root family 1 (Fig. 26(a)). Further increasing the inclination essentially splits the branches into new configurations, as illustrated in Fig. 26(b). These two split branches subsequently formulate the basis for the desirable configurations observed in the baseline case ($i_2 = 30^\circ$), corresponding to min- J TIOTs 1 (Fig. 19) and 3 (Fig. 21), respectively.

Thus, the origin of the three optimal configurations for the baseline scenario can be traced back as follows: two branches originate from the bifurcation of Root family 1 in the coplanar case, and one branch continues from Root family 2. It is worth emphasizing that the geometry associated with Root family 2 does not satisfy the PVT criteria in the coplanar limit (Fig. 23(c)) but evolves to satisfy the necessary conditions as the inclination on the arrival side increases.



(a) Root family 1 at $i_2 = 8^\circ$ and a nearby branch.

(b) Root family 1 at $i_2 = 9^\circ$ and a reconfiguration.

Fig. 26 Bifurcation of Root family 1 between $i_2 = 8^\circ$ and $i_2 = 9^\circ$.

C. Discussions

The results of the present study suggest that viewing TIOTs through a family-based lens provides an alternative and complementary perspective. In particular, the emergence, disappearance, and multiplicity of solution basins observed in the parametric study are naturally interpreted as consequences of bifurcations, collisions, and reconnections of TIOT families, rather than as isolated phenomena tied to specific initial conditions or grid resolutions. This viewpoint emphasizes that the number and structure of locally optimal solutions are global properties of the underlying dynamical and geometric configuration, and are therefore better understood by tracking continuous families than by enumerating discrete optima.

Beyond the specific cases considered here, the proposed framework establishes a foundation for studying the global architecture of orbital transfer problems in a systematic manner. Classical analytically tractable scenarios, such as Hohmann or coaxial transfers, may be revisited from a family-based perspective to reinterpret known optimal solutions as limiting members of broader families. More importantly, the present results suggest that the creation, reconnection, or annihilation of optimal families may be governed by identifiable geometric or dynamical mechanisms, such as the appearance of additional parabolic asymptotes or singular configurations. This observation motivates future research toward semi-analytical characterizations of family bifurcations, aiming to predict when and why new optimal branches arise as orbital parameters vary, without relying solely on exhaustive numerical efforts.

From a practical mission-design standpoint, representing optimal solutions as continuous families offers several advantages over traditional grid-based or pointwise optimization approaches. Rather than isolating a single minimum from a dense grid search (e.g., porkchop plots), the family-based formulation captures the entire neighborhood of optimality, explicitly revealing how nearby configurations vary in both cost and geometry. The width of a family in the angular domain provides a natural measure of robustness: if a nominal launch or maneuver opportunity is missed, adjacent family members immediately suggest alternative near-optimal solutions, e.g., as illustrated in Fig. 22. Furthermore, since families are tracked continuously, the identification of the global minimum is less susceptible to convergence toward spurious local optima, a potential limitation of gradient-based or discretized search methods. In this sense, the proposed framework serves as a bridge between local analytical optimality conditions and the global numerical exploration required for comprehensive and reliable mission planning.

VII. Concluding Remarks

The classical fuel-optimal two-impulse rendezvous problem between Keplerian orbits is revisited from a family-based perspective. Rather than treating optimal transfers as isolated point solutions, the proposed framework analyzes continuous families of stationary transfers, supplying a global view of the optimality landscape connecting two Keplerian orbits. This shift in perspective enables systematic identification, classification, and continuation of optimal solutions across different parameter domains, each revealing complementary structural information. The framework naturally accommodates multiple analytical and numerical strategies, including Hessian-based classification, the Primer Vector Theory conditions, and direct juxtaposition with porkchop plots. By embedding conventional optimal solutions within higher-dimensional families, the approach clarifies the emergence, merging, and disappearance of local minima, saddle points, and disconnected solution basins as orbital parameters vary. From a practical standpoint, the family-based formulation complements existing theory and practice for fuel-optimal transfers by exposing the structure and robustness of nearby solutions, rather than isolating a single optimum. This global characterization is particularly valuable for mission design, where flexibility, sensitivity, and alternative near-optimal options are often as important as the nominal minimum-cost solution.

While the present work primarily introduces and demonstrates the framework, it also lays the foundation for several directions of future research. In particular, a more rigorous treatment of the $\theta = 180^\circ$ singularity, as well as a deeper analysis of bifurcations arising in the coplanar transfer scenario, may enable semi-analytical predictions of family creation and reconnection. Such developments strengthen the link between analytical optimality theory and global numerical exploration of orbital transfer problems.

Appendix A: Gradient Information for the Continuation Scheme

For a differential corrections process to successfully converge to X^* that satisfies the constraints in Eq. (17), the Jacobian matrix $\partial F/\partial X$ is required. Since the constraints themselves define the first-order optimality conditions (gradients of J with respect to X), the required Jacobian involves the second-order derivatives of the cost function J in terms of X .

A. First Order Derivatives: ∇J

The first order derivatives effectively constitute the optimality conditions in Eq. (17). They are evaluated as,

$$\nabla J = \frac{\partial J}{\partial X} = \left[\frac{\partial J}{\partial M_1}, \frac{\partial J}{\partial M_2}, \frac{\partial J}{\partial t} \right]^\top. \quad (29)$$

The derivatives with respect to x_1 and x_2 are trivially supplied via the chain rule that involves $\partial x_1/\partial X$ and $\partial x_2/\partial X$. The first two components require sensitivities of J with respect to the departure and arrival locations that correlate to $\partial v_1^\Gamma/\partial r_1$, $\partial v_1^\Gamma/\partial r_2$, $\partial v_2^\Gamma/\partial r_1$, and $\partial v_2^\Gamma/\partial r_2$. There exist multiple options in the literature for supplying the sensitivities of v_1^Γ and v_2^Γ in terms of r_1 and r_2 within the context of the Lambert problem, leveraging the State Transition Matrix (STM) [44, 45], Lagrange's transfer-time formulation [47], and versine formulation [45]. The algebraic complexity, robustness, and computational time may differ for each of these options. In the current analysis, the STM information is leveraged. While the STM-based Lambert arc sensitivities may be slower as opposed to other geometry-based methods, they offer an advantage in terms of implementation complexity; the STM applies to both elliptic and hyperbolic Lambert arcs. In geometry-based algorithms, the transfer types must be determined a priori. Regardless, any strategies may be leveraged to provide the first-order sensitivities. STM captures the linear variational information along a given Lambert arc Γ as,

$$\begin{bmatrix} \delta r_2 \\ \delta v_2^\Gamma \end{bmatrix} = \begin{bmatrix} \phi_{rr} & \phi_{rv} \\ \phi_{vr} & \phi_{vv} \end{bmatrix} \begin{bmatrix} \delta r_1 \\ \delta v_1^\Gamma \end{bmatrix}, \quad (30)$$

where ϕ is the STM evaluated from T to $T + t$ within the Keplerian dynamics. The subscripts denote the subcomponents of the STM. For example, rv corresponds to the change in the position components upon arrival (δr_2) with respect to the initial velocity variation (δv_1^Γ). Then, following the process from Schumacher Jr et al. [44], the velocity variations are solved in terms of the position variations as [44, 45],

$$\begin{bmatrix} \delta v_1^\Gamma \\ \delta v_2^\Gamma \end{bmatrix} = \begin{bmatrix} -\phi_{rv}^{-1} \phi_{rr} & \phi_{rv}^{-1} \\ \phi_{vr} - \phi_{vv} \phi_{rv}^{-1} \phi_{rr} & \phi_{vv} \phi_{rv}^{-1} \end{bmatrix} \begin{bmatrix} \delta r_1 \\ \delta r_2 \end{bmatrix}, \quad (31)$$

supplying the variation of $\mathbf{v}_{1,2}^\Gamma$ with respect to $\mathbf{r}_{1,2}$. With this information, the first order derivatives of J with respect to $M_{1,2}$ are retrieved as,

$$\frac{\partial J}{\partial M_1} = \frac{\Delta \mathbf{v}_1^\Gamma}{|\Delta \mathbf{v}_1|} \left(\frac{d\mathbf{v}_1}{dM_1} - \frac{\partial \mathbf{v}_1^\Gamma}{\partial \mathbf{r}_1} \frac{d\mathbf{r}_1}{dM_1} \right) + \frac{\Delta \mathbf{v}_2^\Gamma}{|\Delta \mathbf{v}_2|} \left(-\frac{\partial \mathbf{v}_2^\Gamma}{\partial \mathbf{r}_1} \frac{d\mathbf{r}_1}{dM_1} \right), \quad (32)$$

$$\frac{\partial J}{\partial M_2} = \frac{\Delta \mathbf{v}_1^\Gamma}{|\Delta \mathbf{v}_1|} \left(-\frac{\partial \mathbf{v}_1^\Gamma}{\partial \mathbf{r}_2} \frac{d\mathbf{r}_2}{dM_2} \right) + \frac{\Delta \mathbf{v}_2^\Gamma}{|\Delta \mathbf{v}_2|} \left(\frac{d\mathbf{v}_2}{dM_2} - \frac{\partial \mathbf{v}_2^\Gamma}{\partial \mathbf{r}_2} \frac{d\mathbf{r}_2}{dM_2} \right). \quad (33)$$

Here, the derivatives of \mathbf{r} and \mathbf{v} with respect to M are evaluated along the departure and arrival ellipses. As \mathbf{r} , \mathbf{v} are defined within the respective (invariant) Keplerian orbits, they solely depend on their respective mean anomalies; e.g., \mathbf{r}_2 does not depend on M_1 . In the following, the departure side is examined without losing generality. First, Kepler's equation is solved to supply the eccentric anomaly,

$$E_1 = E_1(M_1; e_1), \quad (34)$$

with $\frac{dE_1}{dM_1} = \frac{1}{1 - e_1 \cos E_1}$. Within the perifocal frame (pqw), position and velocity vectors are represented as,

$$\mathbf{r}_1^{pqw} = a_1 \begin{bmatrix} \cos E_1 - e_1 & \sqrt{1 - e_1^2} \sin E_1 & 0 \end{bmatrix}^\top, \quad (35)$$

$$\mathbf{v}_1^{pqw} = \frac{\sqrt{\mu a_1}}{|\mathbf{r}_1|} \begin{bmatrix} -\sin E_1 & \sqrt{1 - e_1^2} \cos E_1 & 0 \end{bmatrix}^\top. \quad (36)$$

Derivatives with respect to M_1 are then,

$$\frac{d\mathbf{r}_1^{pqw}}{dM_1} = a_1 \frac{dE_1}{dM_1} \begin{bmatrix} -\sin E_1 & \sqrt{1 - e_1^2} \cos E_1 & 0 \end{bmatrix}^\top, \quad (37)$$

$$\frac{d\mathbf{v}_1^{pqw}}{dM_1} = \frac{dE_1}{dM_1} \left[-a_1 \left(\frac{\sqrt{\mu a_1} e_1 \sin E_1}{|\mathbf{r}_1|^2} \right) \begin{bmatrix} -\sin E_1 & \sqrt{1 - e_1^2} \cos E_1 & 0 \end{bmatrix}^\top + \frac{\sqrt{\mu a_1}}{|\mathbf{r}_1|} \begin{bmatrix} -\cos E_1 & -\sqrt{1 - e_1^2} \sin E_1 & 0 \end{bmatrix}^\top \right]. \quad (38)$$

Vectors in the perifocal frame and the inertial frame are related via $\mathbf{r}_1 = \mathbf{C}_1 \mathbf{r}_1^{pqw}$. The direction cosine matrix is supplied with the Euler 3-1-3 rotation sequence as,

$$\mathbf{C}_1 = \begin{bmatrix} \cos \Omega_1 \cos \omega_1 - \sin \Omega_1 \sin \omega_1 \cos i_1 & -\cos \Omega_1 \sin \omega_1 - \sin \Omega_1 \cos \omega_1 \cos i_1 & \sin \Omega_1 \sin i_1 \\ \sin \Omega_1 \cos \omega_1 + \cos \Omega_1 \sin \omega_1 \cos i_1 & -\sin \Omega_1 \sin \omega_1 + \cos \Omega_1 \cos \omega_1 \cos i_1 & -\cos \Omega_1 \sin i_1 \\ & \sin \omega_1 \sin i_1 & \cos \omega_1 \sin i_1 & \cos i_1 \end{bmatrix}. \quad (39)$$

Then, the desired sensitivities are supplied as,

$$\frac{d\mathbf{r}_1}{dM_1} = \mathbf{C}_1 \frac{d\mathbf{r}_1^{pqw}}{dM_1}, \quad \frac{d\mathbf{v}_1}{dM_1} = \mathbf{C}_1 \frac{d\mathbf{v}_1^{pqw}}{dM_1}. \quad (40)$$

With these sensitivities in hand, the derivative of J with respect to the time of flight, t , is addressed. This component is more nuanced; specifically, $\partial J/\partial t = \delta J/\delta t + \partial J/\partial M_2 \cdot dM_2/dt$. The first term ($\delta J/\delta t$) captures the explicit dependency on t for a given Lambert arc, and the second term ($\partial J/\partial M_2 \cdot dM_2/dt$) corresponds to the indirect impact where t changes the arrival location. In the time-variable formulation, the variation equation along the Lambert arc results in,

$$\begin{bmatrix} \delta \mathbf{r}_2 \\ \delta \mathbf{v}_2^\Gamma \end{bmatrix} = \begin{bmatrix} \phi_{rr} & \phi_{rv} & \frac{d\mathbf{r}_2}{d\tau} \\ \phi_{vr} & \phi_{vv} & \frac{d\mathbf{v}_2^\Gamma}{d\tau} \end{bmatrix} \begin{bmatrix} \delta \mathbf{r}_1 \\ \delta \mathbf{v}_1^\Gamma \\ \delta t \end{bmatrix}. \quad (41)$$

Recall that τ is a generic time variable. In evaluating $\delta J/\delta t$, variations in $\mathbf{r}_{1,2}$ do not occur, i.e., $\delta \mathbf{r}_{1,2} = \mathbf{0}$. Thus,

$$\frac{\delta \mathbf{v}_1^\Gamma}{\delta t} = -\phi_{rv}^{-1} \frac{d\mathbf{r}_2}{d\tau} = -\phi_{rv}^{-1} \mathbf{v}_2^\Gamma, \quad (42)$$

$$\frac{\delta \mathbf{v}_2^\Gamma}{\delta t} = -\phi_{vv} \phi_{vr}^{-1} \frac{d\mathbf{r}_2}{d\tau} + \frac{d\mathbf{v}_2^\Gamma}{d\tau}, \quad (43)$$

from a straightforward extension of Arora et al. [45]***. The explicit sensitivity of J with respect to t is then,

$$\frac{\delta J}{\delta t} = -\frac{\Delta \mathbf{v}_1^\Gamma}{|\Delta \mathbf{v}_1|} \frac{\delta \mathbf{v}_1^\Gamma}{\delta t} - \frac{\Delta \mathbf{v}_2^\Gamma}{|\Delta \mathbf{v}_2|} \frac{\delta \mathbf{v}_2^\Gamma}{\delta t}. \quad (44)$$

As units of $\partial J/\partial M$ are different from $\delta J/\delta t$ (or $\partial J/\partial t$), a proper scaling for $\delta J/\delta t$ reduces potential numerical instabilities. In the current analysis, t is divided by 1000 seconds to supply an arbitrary nondimensional time unit; such quantities may be redefined according to the periods of the departure and arrival ellipses.

B. Second Order Derivatives: $\nabla^2 J$

Second-order derivatives of J serve two purposes: (1) classifying stationary solutions as minima, maxima, or saddle points via the Hessian eigenvalues (Eq. (22)), and (2) constructing the Jacobian $\partial \mathbf{F}/\partial \mathbf{X}$ required by the differential

***While in Arora et al. [45] the departure and arrival epochs are separate variables and sensitivities to these epochs are separately supplied, the impact of epochs is considered through $M_{1,2}$ in the current analysis and only the sensitivity to t is required, resulting in rather simple expressions as in Eqs. (42)-(43).

corrections process to enforce Eq. (17). The latter is evaluated as,

$$\frac{\partial \mathbf{F}}{\partial \mathbf{X}} = \begin{bmatrix} \frac{\partial^2 J}{\partial x_1 \partial M_1} & \frac{\partial^2 J}{\partial x_1 \partial M_2} & \frac{\partial^2 J}{\partial x_1 \partial t} \\ \frac{\partial^2 J}{\partial x_2 \partial M_1} & \frac{\partial^2 J}{\partial x_2 \partial M_2} & \frac{\partial^2 J}{\partial x_2 \partial t} \end{bmatrix}. \quad (45)$$

Multiple strategies exist to (semi-)analytically supply the Hessian information. Examples include the state transition tensors [48], differential algebra [49, 50], and geometry-based methods, e.g., vercosine formulation as disclosed in the appended Fortran code from Russell [18]. While these (semi-)analytical second-order derivatives may be considered more accurate, it is true that they entail additional implementation complexities. In the current analysis, such information is numerically delivered with the central finite differencing technique, perturbing with a small number $h = 1 \cdot 10^{-7}$. For example,

$$\frac{\partial^2 J}{\partial M_1 \partial M_2} \Big|_{(M_1^*, M_2^*, t^*)} \approx \left(\frac{\partial J}{\partial M_1} \Big|_{(M_1^*, M_2^* + h, t^*)} - \frac{\partial J}{\partial M_1} \Big|_{(M_1^*, M_2^* - h, t^*)} \right) / (2h). \quad (46)$$

In the following numerical examples, this differencing technique is sufficient to deliver the required second-order derivatives in Eqs. (22)-(45). Thus, exploring alternatives for delivering the second-order derivatives remains out of the scope for the current analysis.

Appendix B: Asymptotic Behavior at $t \rightarrow 0$ in the Angular Domain

The asymptotic case at $t \rightarrow 0$ implies an instantaneous change in position between two orbits at M_1, M_2 with $J \rightarrow \infty$ with $|v_1^\Gamma|, |v_2^\Gamma|$ approaching ∞ . In such a limiting case, the following relationship holds,

$$J \approx |v_1^\Gamma| + |v_2^\Gamma| \approx 2 \frac{s^\Gamma}{t}, \quad (47)$$

where s^Γ is the distance traveled along the Lambert arc as $t \rightarrow 0$. Two possible scenarios emerge,

$$s^\Gamma = |\mathbf{r}_1(M_1) - \mathbf{r}_2(M_2)|, \quad \text{The solution does not go through the central body (short transfer),} \quad (48)$$

$$= |\mathbf{r}_1(M_1)| + |\mathbf{r}_2(M_2)|, \quad \text{The solution goes through the central body (long transfer).} \quad (49)$$

In the former, the Lambert arc consists of one (nearly-)straight line. In the latter, the arc results in two (nearly-)straight lines that instantaneously change direction with the intersection with the central body^{†††}. Thus, the optimality constraint

^{†††}At its limiting case, $t \rightarrow 0$ forces the trajectory to approach the central body (Earth) in a nearly rectilinear fashion; then, the central body pulls the trajectory with a turn angle that approximates an impulsive burn of infinite magnitude at the center of the body; obviously, the collision at the surface is ignored for a theoretical construction of such transfers.

from Eq. (23) interchanges with,

$$\left[\frac{ds^\Gamma}{dM_1}, \frac{ds^\Gamma}{dM_2} \right]^\top = \mathbf{0}, \quad (50)$$

i.e., combinations of M_1, M_2 that result in stationary distance traveled are searched. For illustration, consider Fig. 27. Figure 27(a) takes a sample value of $t = 10$ seconds, a very small value to approximate the $t \rightarrow 0$ behavior. A contour plot of J is generated for each combination of M_1, M_2 , assuming short transfers. While all Lambert arcs are associated with impractical J values, it is obvious that variations in J are still present. The contour plot in Fig. 27(b) depicts the distance $s^\Gamma = |\mathbf{r}_1 - \mathbf{r}_2|$ connecting two locations; two contour plots in Figs. 27(a) and 27(b) demonstrate nearly identical behaviors. The long transfers are examined in Fig. 28. Figure 28(a) demonstrates a contour plot of J at $t = 10$ seconds. It is clear that the function is an independent combination of M_1 and M_2 ; at the center of the plot, $M_1 = M_2 = \pi$, the Lambert arc connects the apogees of two orbits. Thus, maximal distance is traveled and results in the largest cost J . Similarly, $M_1 = M_2 = 0$ results in minimally traveled distance and the lowest cost J . The Lambert arc corresponding to the maximal cost is illustrated in Fig. 28(b) within the Earth-centered inertial frame. The dotted lines denote the direction of the eccentricity vectors of the two orbits. Clearly, the Lambert arc links apogees of the orbits. In denoting these asymptotic cases of the optimal Lambert families at $t \rightarrow 0$, following notation is introduced,

$$0_{b,c}^a. \quad (51)$$

Identical to Eq. (25), $a = s, l$ denote the short and long transfer scenarios. The Hessian information is classified by b with m, M, σ denoting the local minimum, maximum, and saddle, respectively. Finally, $c \geq 1$ is the index to enumerate multiple cases under the same category. The asymptotic locations for the baseline scenario in Table 1 are included in Table 7.

Two additional interesting insights exist for the $t \rightarrow 0$ asymptotic case. First, it serves as asymptotes for the reverse order transfers as well. Moreover, as the velocity along the transfer arc approaches infinity, the asymptotic behaviors ignore all the gravitational influences; thus, the asymptotic behaviors likely extrapolate to more complex dynamical environment, e.g., the Circular Restricted Three-Body Problem (CR3BP). A family of TIOTs in the angular domain may be initiated whenever the distance between departure and arrival (periodic) orbits is stationary with respect to the nearby variations.

Table 7 Approximate asymptotic stationary points ($t \rightarrow 0$) in the angular domain for the baseline scenario (Table 1)

Label	M_1 [rad]	M_2 [rad]
$0_{M,1}^s$	3.02	4.71
$0_{\sigma,1}^s$	5.65	0.75
$0_{\sigma,2}^s$	2.32	0.69
$0_{\sigma,3}^s$	5.65	3.96
$0_{m,1}^s$	0.57	5.53
$0_{m,2}^s$	4.21	2.26
$0_{M,1}^l$	π	π
$0_{\sigma,1}^l$	π	0
$0_{\sigma,2}^l$	0	π
$0_{m,1}^l$	0	0

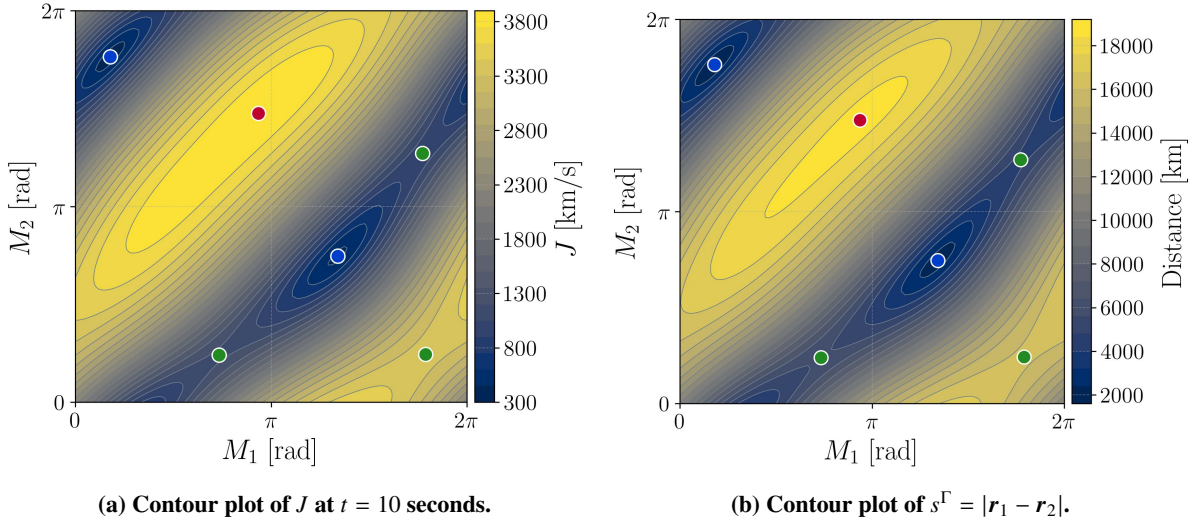


Fig. 27 Relationship between cost (J) and distance (s^Γ) at $t \rightarrow 0$ for $d_1 = s$, with colored dots indicating Hessian information (Table 2).

Appendix C: Parabolic Lambert Arcs

Along a parabolic arc connecting the departure and arrival orbits, the conic equation is given by

$$r_i = \frac{p}{1 + \cos f_i}, \quad \text{for } i = 1, 2, \quad (52)$$

where r_i denotes the radial distance from the central body at the departure and arrival points, respectively. The quantities p and f_i represent the semi-latus rectum and the true anomaly at each endpoint. Expanding this relation yields

$$r_1 (1 + \cos f_1) = r_2 (1 + \cos f_2) = r_2 (1 + \cos(f_1 + \theta)), \quad \theta = \theta^s, \theta^l, \quad (53)$$

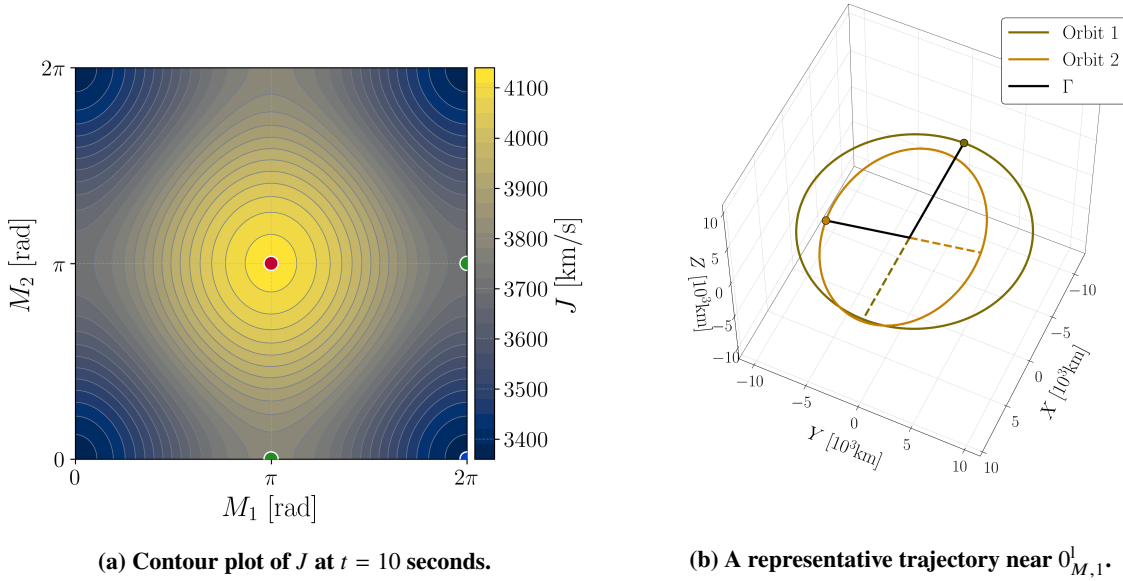


Fig. 28 Asymptotic characteristics at $t \rightarrow 0$ ($d_1 = 1$), with colored dots indicating Hessian information (Table 2).

where the transfer angle θ is defined as

$$\theta^s = \arccos\left(\frac{\mathbf{r}_1^\top \mathbf{r}_2}{r_1 r_2}\right), \quad \theta^l = 2\pi - \theta^s, \quad (54)$$

corresponding to the short and long transfers, respectively, i.e., $d_1 = s, l$. Rearranging Eq. (53) renders

$$(r_1 - r_2 \cos \theta) \cos f_1 + r_2 \sin \theta \sin f_1 = r_2 - r_1, \quad (55)$$

which may be expressed in a more compact form as

$$\cos(f_1 - \delta) = \frac{C}{\sqrt{A^2 + B^2}}, \quad (56)$$

with

$$A = r_1 - r_2 \cos \theta, \quad B = r_2 \sin \theta, \quad C = r_2 - r_1, \quad \delta = \arctan_2(B, A). \quad (57)$$

Here, $\arctan_2(\cdot)$ denotes the four-quadrant inverse tangent. As discussed in Section IV, parabolic Lambert arcs are employed to examine stationary transfer geometries in terms of the cost function J at $t \rightarrow \infty$. For a given combination

of departure and arrival positions, \mathbf{r}_1 and \mathbf{r}_2 , two solutions exist for Eq. (56) as

$$f_1 = \delta \pm \arccos\left(\frac{C}{\sqrt{A^2 + B^2}}\right), \quad (58)$$

where the sign is selected to yield the transfer geometry corresponding to the parabolic limit $t \rightarrow \infty$. This limiting behavior occurs only when the trajectory traverses $f = \pi$, a condition that uniquely determines the admissible branch and removes the sign ambiguity in Eq. (58) by selecting the positive sign. Once f_1 is determined, the arrival true anomaly follows as $f_2 = f_1 + \theta$, and the semi-latus rectum is given by $p = r_1(1 + \cos f_1)$. These quantities fully determine the parabolic Lambert arc. Consequently, the transfer cost J may be computed for each sampled combination of \mathbf{r}_1 and \mathbf{r}_2 , yielding contour plots such as those demonstrated in Figs. 2(b) (short transfers) and 3(b) (long transfers) for the baseline transfer scenario (Table 1).

Appendix D: Proof of Proposition 1

First, consider the 3 by 3 block matrix, $\phi_{r\mathbf{v}}$, from the STM (Eq. (21)) as $t \rightarrow \infty$. With the singular value decomposition, $\phi_{r\mathbf{v}} = \mathbf{U}\mathbf{S}\mathbf{V}^\top$ with standard definitions; \mathbf{U} , \mathbf{V} are left and right singular vectors, respectively, and \mathbf{S} is a diagonal matrix with singular values. Within the Keplerian dynamics, only the largest singular value σ_1 grows linearly with time ($O(t)$) [51, 52], corresponding to the phase shift due to the change in the semi-major axis; the other two singular values are on the order of $O(1)$ from the super-integrable nature of the dynamics. With the linear time growth, as $t \rightarrow \infty$, $\phi_{r\mathbf{v}}$ approaches the following rank-1 matrix,

$$\phi_{r\mathbf{v}} \rightarrow \sigma_1 \mathbf{U}_1 \mathbf{V}_1^\top, \quad (59)$$

where \mathbf{U}_1 , \mathbf{V}_1 are left and right singular vectors corresponding to σ_1 , respectively. The right singular vector \mathbf{V}_1 is determined via the gradient of semi-major axis (a) with respect to the initial velocity along the transfer arc, \mathbf{v}_1^Γ ; such a direction incurs the largest change in a without variation in the initial \mathbf{r} . As such, $\mathbf{V}_1 = \mathbf{v}_1^\Gamma / |\mathbf{v}_1^\Gamma|$. The change in the final position vector with the initial variation into this velocity-aligned direction is,

$$\delta \mathbf{r}(t) = \frac{\partial \mathbf{r}}{\partial M} \delta M = \frac{\mathbf{v}^\Gamma(t)}{n} \delta n \cdot t = -\frac{3a}{\mu} \mathbf{v}^\Gamma(t) (\mathbf{v}_1^\Gamma \cdot \delta \mathbf{v}_1^\Gamma) t, \quad (60)$$

where $\delta n = -\frac{3na}{\mu} (\mathbf{v}_1^\Gamma \cdot \delta \mathbf{v}_1^\Gamma)$ is leveraged. Then, Eq. (60) is re-written^{***} as,

$$\frac{\partial \mathbf{r}_2}{\partial \mathbf{v}_1^\Gamma} \sim \frac{3a |\mathbf{v}_1^\Gamma| |\mathbf{v}_2^\Gamma|}{\mu} \begin{pmatrix} -\mathbf{v}_2^\Gamma \\ |\mathbf{v}_2^\Gamma| \end{pmatrix} \begin{pmatrix} \mathbf{v}_1^\Gamma \\ |\mathbf{v}_1^\Gamma| \end{pmatrix}^\top t, \quad (61)$$

^{***}From a similar logic, any block matrix of the STM may be decomposed into this most stretching direction for $t \rightarrow \infty$.

noting that $\mathbf{v}^\Gamma(t) = \mathbf{v}_2^\Gamma$. Comparing Eq. (61) and (60), it is clear that

$$\sigma_1 = \frac{3a|\mathbf{v}_1^\Gamma||\mathbf{v}_2^\Gamma|}{\mu}t, \quad \mathbf{U}_1 = -\frac{\mathbf{v}_2^\Gamma}{|\mathbf{v}_2^\Gamma|}, \quad \mathbf{V}_1 = \frac{\mathbf{v}_1^\Gamma}{|\mathbf{v}_1^\Gamma|}. \quad (62)$$

Now, Eq. (42) renders the following at $t \rightarrow \infty$,

$$\frac{\delta \mathbf{v}_1^\Gamma}{\delta t} = |\mathbf{v}_2^\Gamma| \mathbf{V} \mathbf{S}^{-1} \mathbf{U}^\top \mathbf{U}_1 \sim \frac{|\mathbf{v}_2^\Gamma|}{\sigma_1} \mathbf{V}_1 \rightarrow \mathbf{0}, \quad \text{as } t \rightarrow \infty, \quad (63)$$

as $\sigma_1 \rightarrow \infty$ at $t \rightarrow \infty$. With the STM propagated in reverse time from the final to the initial points along the Lambert arc Γ , it is trivial to demonstrate $\frac{\delta \mathbf{v}_2^\Gamma}{\delta t} \rightarrow \mathbf{0}$ as well. With these zero vectors, Eq. (44) also renders a zero vector, i.e., sensitivity of J with respect to t disappears with $t \rightarrow \infty$. At such an asymptotic case, the two conditions in Eqs. (27)-(28) become identical to conditions in Eq. (23). Thus, the $T - t$ domain approaches $M_1 - M_2$ domain at $t \rightarrow \infty$.

Appendix E: Application of the Framework to the Angular Domain

This appendix demonstrates the application of the TIOT family framework, developed in Section V, to the angular domain. In contrast to the temporal domain analyzed in the main body, the present appendix focuses on families parameterized within the $M_1 - M_2$ domain. Starting seeds are supplied from the asymptotic behaviors associated with the limits $t \rightarrow 0, \infty$. Within the $M_1 - M_2$ domain, these seeds are illustrated in Figs. 27(a) ($t \rightarrow 0$, short transfers), 28(a) ($t \rightarrow 0$, long transfers), 2(a) ($t \rightarrow \infty$, short transfers), and 3(a) ($t \rightarrow \infty$, long transfers). Utilizing the continuation scheme from Section III.B, TIOT families are traced each of these seeds. Through this process, a total of 16 unique TIOT families are identified in the angular domain. These families are indexed in Table 8, along with their associated asymptotic behaviors and connections to other families. The last column of Table 8 displays the colors that visualize each family within the three-dimensional ($M_1 - M_2 - t$) space in Fig. 29. Overall, the angular domain results confirm that the proposed framework is not restricted to the temporal domain formulation. The same seeding, continuation, and classification procedures apply directly, yielding a consistent family-based description of TIOTs across different optimality domains.

Table 8 Summary of indexed TIOT families in the angular domain for the baseline scenario (Table 1)

Family No.	End point 1	End point 2	Connections (if any)	Color
1	$\infty_{m,2}^1$	π_2	Family 14	
2	$\infty_{m,1}^1$	π_1	Family 8	
3	$\infty_{\sigma,1}^1$	π_1	-	
4	$\infty_{\sigma,2}^1$	$0_{\sigma,1}^1$	-	
5	$\infty_{\sigma,3}^1$	π_2	-	
6	$\infty_{M,1}^1$	π_1	Family 9	
7	$\infty_{\sigma,2}^s$	$0_{\sigma,1}^s$	-	
8	$\infty_{\sigma,4}^s$	π_1	Family 2	
9	$\infty_{\sigma,1}^s$	π_1	Family 6	
10	$\infty_{\sigma,3}^s$	$0_{\sigma,2}^s$	-	
11	$0_{m,1}^l$	$0_{\sigma,2}^l$	-	
12	$0_{M,1}^l$	π_2	-	
13	$0_{\sigma,3}^s$	$0_{m,1}^s$	-	
14	$0_{m,2}^s$	π_2	Family 1	
15	$0_{M,1}^s$	π_2	Family 16	
16	π_1	π_2	Family 15	

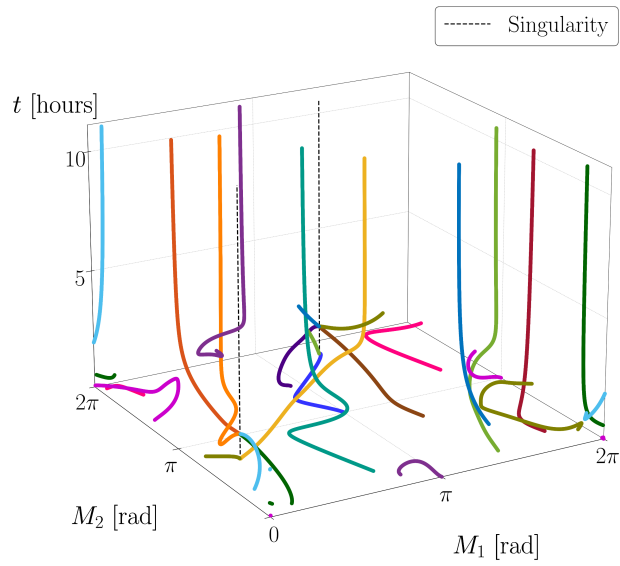
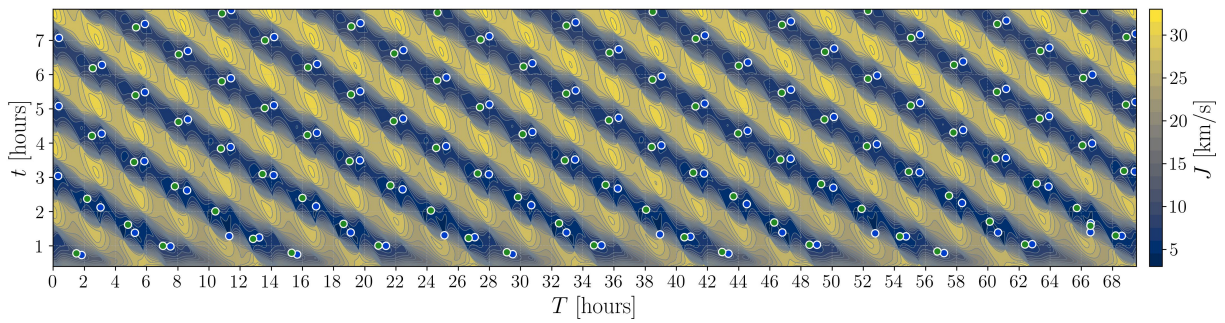


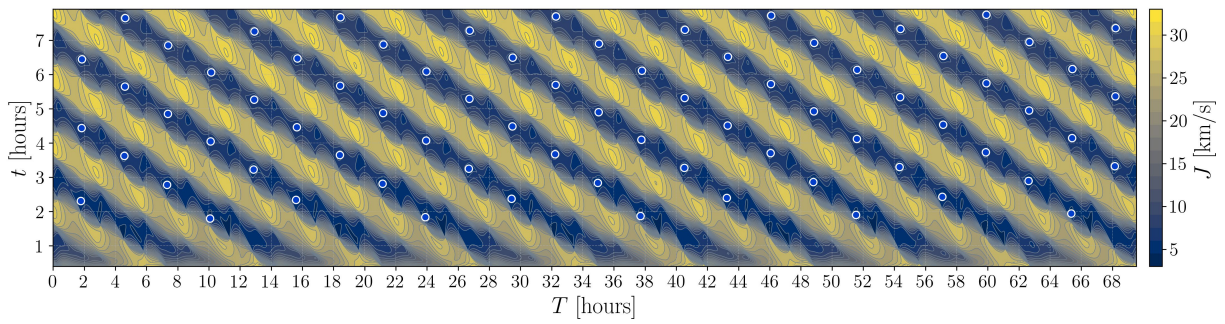
Fig. 29 Global structure of TIOT families in the angular domain colored by their indices.

Appendix F: Projection of Temporal Domain Families onto Porkchop Plots

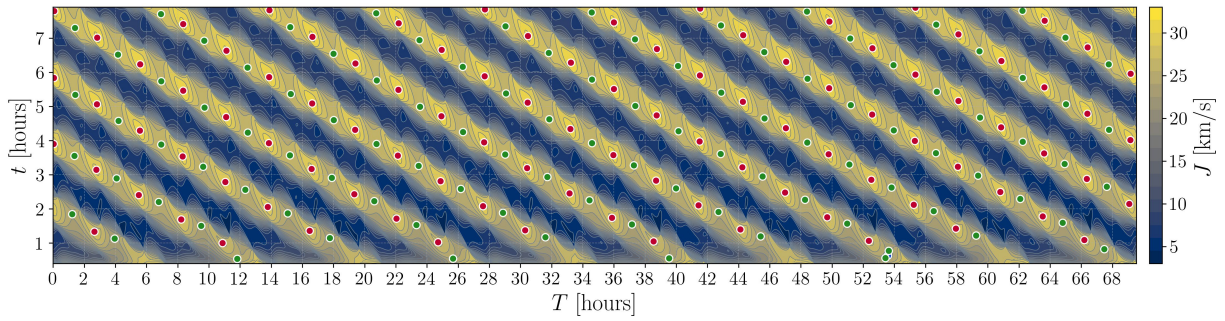
Figure 30 presents the projection of the families obtained in the temporal domain onto porkchop plots. The corresponding orbital geometries for each family are supplied in Fig. 18.



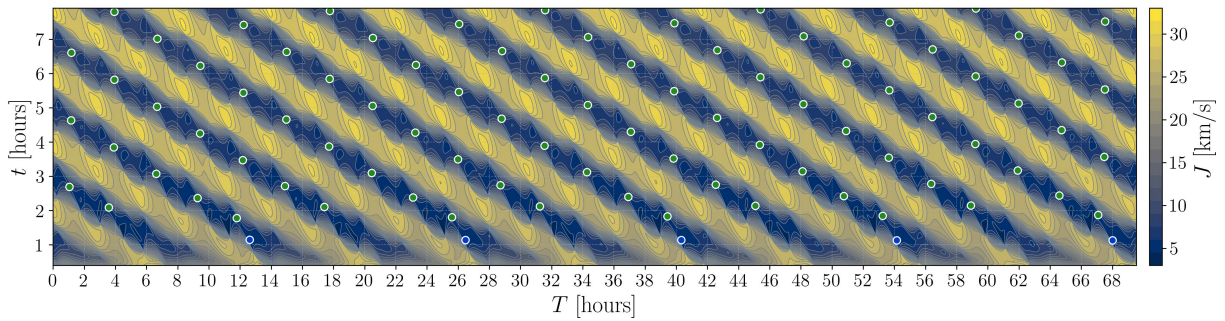
(a) Family 1.



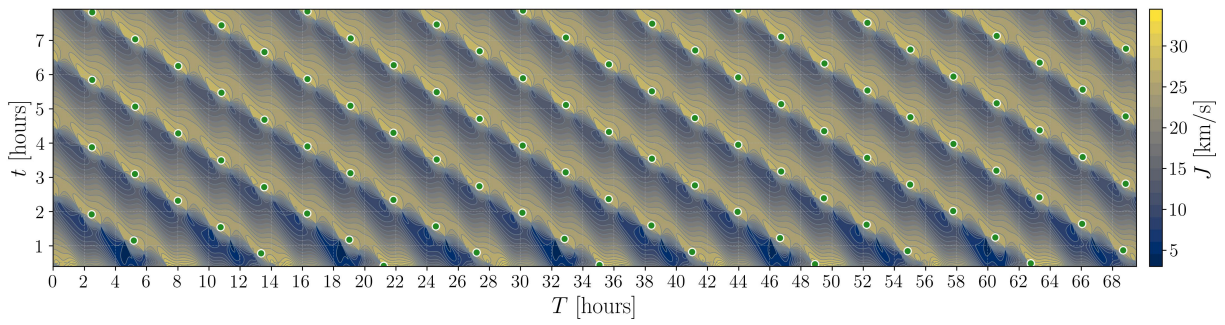
(b) Family 2.



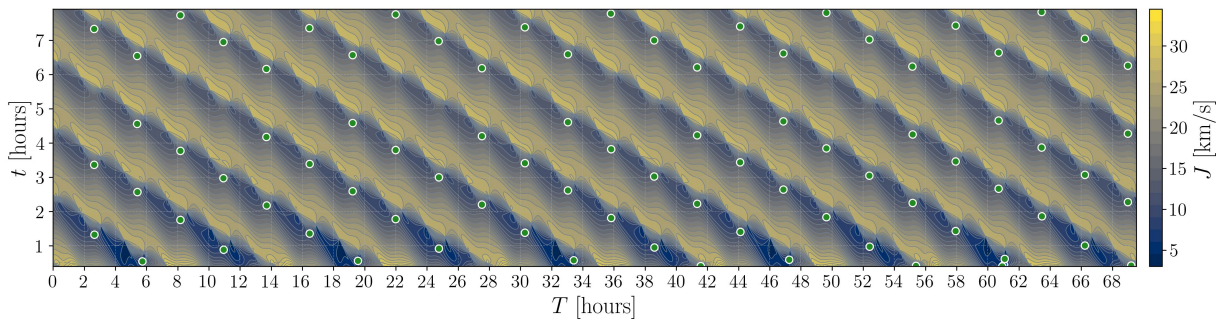
(c) Family 3.



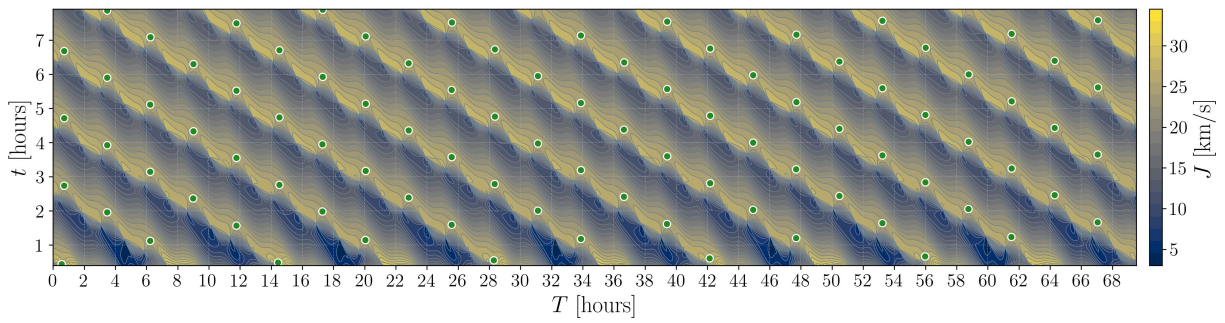
(d) Family 4.



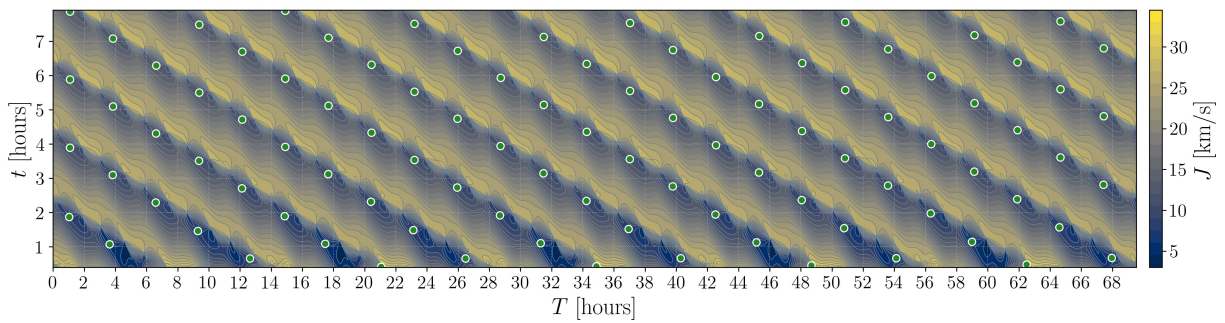
(e) Family 5.



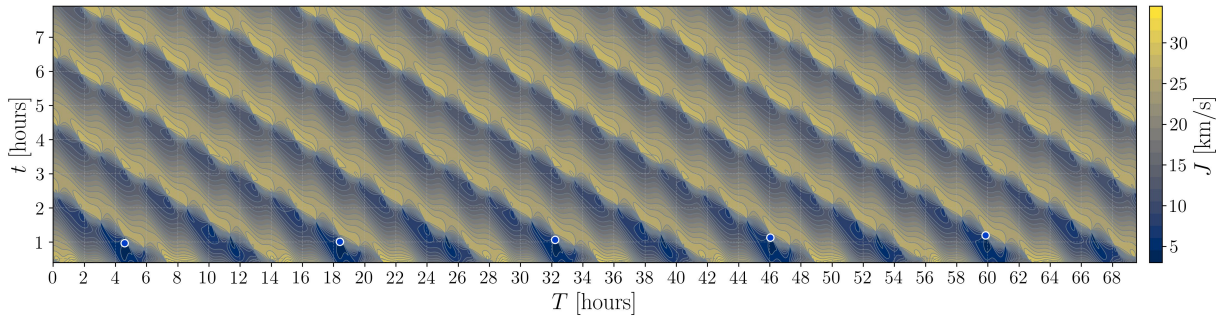
(f) Family 6.



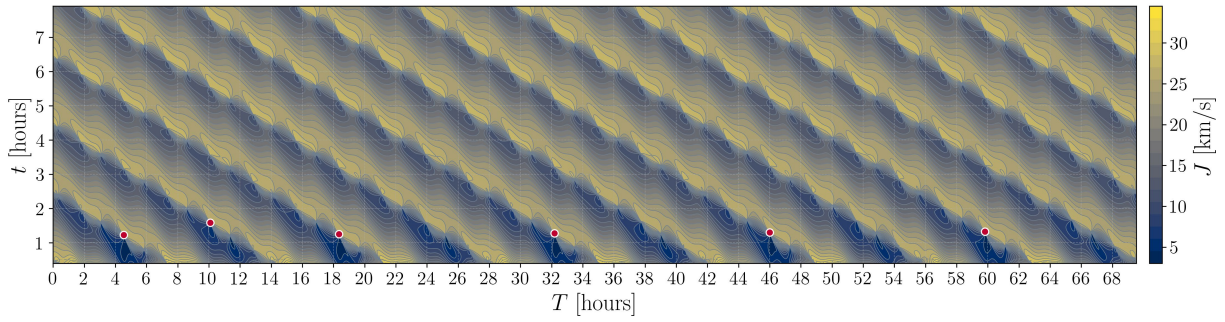
(g) Family 7.



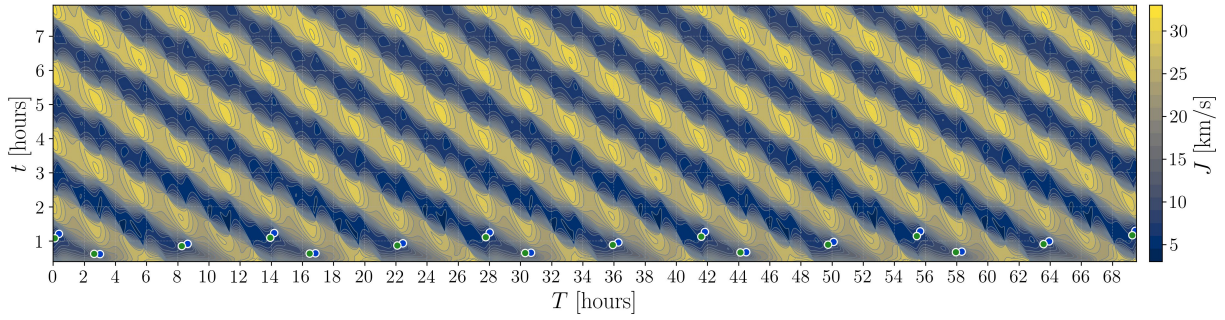
(h) Family 8.



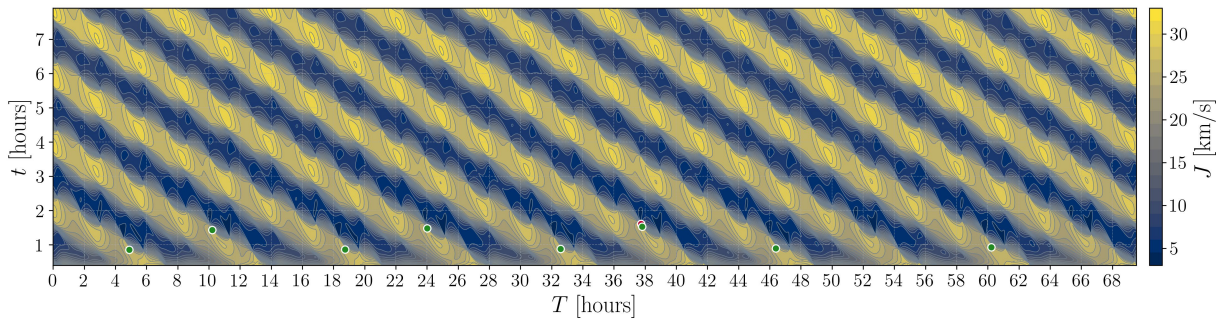
(i) Family 9.



(j) Family 10.



(k) Family 11.



(l) Family 12.

Fig. 30 Visual catalog of the 12 identified TIOT families (Fig. 14) projected onto porkchop plots for the baseline scenario (Table 5).

Funding Sources

Dr. Beom Park was partially supported by the Apollo 11 Postdoctoral Fellowship from the School of Aeronautics and Astronautics at Purdue University, USA. This work was supported by the InnoCORE program of the Ministry of Science and ICT of the Republic of Korea (KAIST N10250155).

Acknowledgments

Dr. Park would like to thank the members of the Strategic Aerospace Initiative (SAI) research group at KAIST for their hospitality and invaluable feedback during his stay in the summer of 2025. Dr. Park also acknowledges valuable discussions with Dr. Mitch Dominguez on the continuation scheme.

References

- [1] Hohmann, W., “The Attainability of Heavenly Bodies,” NASA Technical Translation F-44, National Aeronautics and Space Administration, Washington, D.C., Nov. 1960. Translated from the German original *Die Erreichbarkeit der Himmelskörper* (R. Oldenbourg, Munich and Berlin, 1925).
- [2] Gobetz, F. W., and Doll, J. R., “A Survey of Impulsive Trajectories,” *AIAA Journal*, Vol. 7, No. 5, 1969, pp. 801–834. doi:10.2514/3.5231.
- [3] Walsh, M. T., and Peck, M. A., “Survey of Methods for Calculating Impulsive ΔV -Minimizing Orbit Transfer Maneuvers,” *AIAA Paper 2020–1923*, Jan 2020. doi:10.2514/6.2020-1923.
- [4] Morante, D., Rivo, M. S., and Soler, M., “A Survey on Low-Thrust Trajectory Optimization Approaches,” *Aerospace*, Vol. 8, No. 3, 2021, p. 88. doi:10.3390/aerospace8030088.
- [5] Vinh, N. X., Kuo, S. H., and Marchal, C., “Optimal Time-Free Nodal Transfers Between Elliptical Orbits,” *Acta Astronautica*, Vol. 17, No. 8, 1988, pp. 875–880. doi:10.1016/0094-5765(88)90170-1.
- [6] Vallado, D. A., *Fundamentals of Astrodynamics and Applications*, Vol. 5, Microcosm Press, Torrance, CA, 2022.
- [7] Lawden, D. F., *Optimal Trajectories for Space Navigation*, Butterworths, London, 1963.
- [8] Longuski, J. M., Guzmán, J. J., and Prussing, J. E., *Optimal Control with Aerospace Applications*, Space Technology Library, Vol. 32, Springer, New York, 2014. doi:10.1007/978-1-4614-8945-0.
- [9] Holzinger, M. J., Chow, C. C., and Garretson, P., “A Primer on Cislunar Space,” Tech. Rep. AFRL 2021-1271, Air Force Research Laboratory, 2021.
- [10] Yang, B., Li, S., Feng, J., and Vasile, M., “Fast Solver for J2-Perturbed Lambert Problem Using Deep Neural Network,” *Journal of Guidance, Control, and Dynamics*, Vol. 45, No. 5, 2022, pp. 875–884. doi:10.2514/1.G006091.

- [11] Prussing, J. E., “Optimal Impulsive Linear Systems: Sufficient Conditions and Maximum Number of Impulses,” *The Journal of the Astronautical Sciences*, Vol. 43, No. 2, 1995, pp. 195–206.
- [12] McMahon, J. W., and Scheeres, D. J., “Linearized Lambert’s Problem Solution,” *Journal of Guidance, Control, and Dynamics*, Vol. 39, No. 10, 2016, pp. 2205–2218. doi:10.2514/1.G000394.
- [13] Saloglu, K., Taheri, E., and Landau, D., “Existence of Infinitely Many Optimal Iso-Impulse Trajectories in Two-Body Dynamics,” *Journal of Guidance, Control, and Dynamics*, Vol. 46, No. 10, 2023, pp. 1945–1962. doi:10.2514/1.G007409.
- [14] Saloglu, K., and Taheri, E., “Classification and Feasibility Assessment of Infinitely Many Iso-Impulse Three-Dimensional Trajectories,” *The Journal of the Astronautical Sciences*, Vol. 72, Sep 2025, p. 54. doi:10.1007/s40295-025-00528-0.
- [15] Zhu, Z., Gan, Q., Yang, X., and Gao, Y., “Solving Fuel-Optimal Low-Thrust Orbital Transfers with Bang-Bang Control Using a Novel Continuation Technique,” *Acta Astronautica*, Vol. 137, Aug 2017, pp. 98–113. doi:10.1016/j.actaastro.2017.03.032.
- [16] Bang, J., and Ahn, J., “Two-Phase Framework for Near-Optimal Multi-Target Lambert Rendezvous,” *Advances in Space Research*, Vol. 61, No. 5, 2018, pp. 1273–1285. doi:10.1016/j.asr.2017.12.025.
- [17] Battin, R. H., *An Introduction to the Mathematics and Methods of Astrodynamics*, American Institute of Aeronautics and Astronautics, Reston, VA, 1999. doi:10.2514/4.861543.
- [18] Russell, R. P., “On the Solution to Every Lambert Problem,” *Celestial Mechanics and Dynamical Astronomy*, Vol. 131, Oct 2019, p. 50. doi:10.1007/s10569-019-9927-z.
- [19] Lancaster, E. R., “Solution of Lambert’s problem for short arcs,” *Celestial Mechanics*, Vol. 2, Mar 1970, pp. 60–63. doi:10.1007/BF01230450.
- [20] Gooding, R. H., “A Procedure for the Solution of Lambert’s Orbital Boundary-Value Problem,” *Celestial Mechanics and Dynamical Astronomy*, Vol. 48, Jun 1990, pp. 145–165. doi:10.1007/BF00049511.
- [21] Izzo, D., “Revisiting Lambert’s Problem,” *Celestial Mechanics and Dynamical Astronomy*, Vol. 121, Jan 2015, pp. 1–15. doi:10.1007/s10569-014-9587-y.
- [22] Hazelrigg Jr., G. A., “Globally Optimal Impulsive Transfers via Green’s Theorem,” *Journal of Guidance, Control, and Dynamics*, Vol. 7, No. 4, 1984, pp. 462–470. doi:10.2514/3.19879.
- [23] Prussing, J. E., “Simple Proof of the Global Optimality of the Hohmann Transfer,” *Journal of Guidance, Control, and Dynamics*, Vol. 15, No. 4, 1992, pp. 1037–1038. doi:10.2514/3.20941.
- [24] Palmore, J., “An Elementary Proof of the Optimality of Hohmann Transfers,” *Journal of Guidance, Control, and Dynamics*, Vol. 7, No. 5, 1984, pp. 629–630. doi:10.2514/3.56375.
- [25] Baker, J. M., “Orbit Transfer and Rendezvous Maneuvers Between Inclined Circular Orbits,” *Journal of Spacecraft and Rockets*, Vol. 3, No. 8, 1966, pp. 1216–1220. doi:10.2514/3.28630.

- [26] Pontani, M., “Simple Method to Determine Globally Optimal Orbital Transfers,” *Journal of Guidance, Control, and Dynamics*, Vol. 32, No. 3, 2009, pp. 899–914. doi:10.2514/1.38143.
- [27] Zaborsky, S., “Analytical Solution of Two-Impulse Transfer Between Coplanar Elliptical Orbits,” *Journal of Guidance, Control, and Dynamics*, Vol. 37, No. 3, 2014, pp. 996–1000. doi:10.2514/1.62072.
- [28] Lacruz, E., and Ángeles, D., “Coaxial Transfer Orbit Between Noncoplanar and Noncoaxial Elliptical Orbits,” *Journal of Guidance, Control, and Dynamics*, Vol. 47, No. 4, 2024, pp. 787–796. doi:10.2514/1.G007872.
- [29] Gooding, R. H., “On the Solution of Lambert’s Orbital Boundary Value Problem,” Tech. Rep. 88027, Royal Aerospace Establishment, Farnborough, Hante, Apr 1988.
- [30] Battin, R. H., and Vaughan, R. M., “An Elegant Lambert Algorithm,” *Journal of Guidance, Control, and Dynamics*, Vol. 7, No. 6, 1984, pp. 662–670. doi:10.2514/3.19910.
- [31] McCue, G. A., “Optimum Two-Impulse Orbital Transfer and Rendezvous Between Inclined Elliptical Orbits,” *AIAA Journal*, Vol. 1, No. 8, 1963, pp. 1865–1872. doi:10.2514/3.1937.
- [32] Lee, G., “An Analysis of Two-Impulse Orbital Transfer,” *AIAA Journal*, Vol. 2, No. 10, 1964, pp. 1767–1773. doi:10.2514/3.2663.
- [33] McCue, G. A., and Bender, D. F., “Numerical Investigation of Minimum Impulse Orbital Transfer,” *AIAA Journal*, Vol. 3, No. 12, 1965, pp. 2328–2334. doi:10.2514/3.3363.
- [34] Stark, H. M., “Optimum Trajectories Between Two Terminals in Space,” *ARS Journal*, Vol. 31, No. 2, 1961, pp. 261–263. doi:10.2514/8.5447.
- [35] Abdelkhalik, O., and Mortari, D., “ N -Impulse Orbit Transfer Using Genetic Algorithms,” *Journal of Spacecraft and Rockets*, Vol. 44, No. 2, 2007, pp. 456–459. doi:10.2514/1.24701.
- [36] Pontani, M., and Conway, B. A., “Particle Swarm Optimization Applied to Impulsive Orbital Transfers,” *Acta Astronautica*, Vol. 74, May–Jun 2012, pp. 141–155. doi:10.1016/j.actaastro.2011.09.007.
- [37] Jezewski, D. J., and Rozendaal, H. L., “An Efficient Method for Calculating Optimal Free-Space N -Impulse Trajectories,” *AIAA Journal*, Vol. 6, No. 11, 1968, pp. 2160–2165. doi:10.2514/3.4949.
- [38] Small, H. W., “Minimum N -impulse Time-Free Transfers Between Elliptic Orbits,” *AIAA Journal*, Vol. 9, No. 4, 1971, pp. 594–599. doi:10.2514/3.6235.
- [39] Prussing, J. E., “A Class of Optimal Two-Impulse Rendezvous Using Multiple-Revolution Lambert Solutions,” *The Journal of the Astronautical Sciences*, Vol. 48, Jun 2000, pp. 131–148. doi:10.1007/BF03546273.
- [40] Taheri, E., and Junkins, J. L., “How Many Impulses Redux,” *The Journal of the Astronautical Sciences*, Vol. 67, Jun 2020, pp. 257–334. doi:10.1007/s40295-019-00203-1.

- [41] McCarthy, B., Scheuerle, S., Zimovan-Spreen, E., Williams, D., Davis, D., and Howell, K., “Rephasing and Loitering Strategies in the Gateway Near Rectilinear Halo Orbit,” *AAS/AAIA Astrodynamics Specialist Conference*, 2023, pp. AAS 23–200.
- [42] Gul, R., Dominguez, M., Dai, R., and Howell, K., “Feature Learning Based Optimal Control Method for Cislunar Trajectory Design,” *AIAA Paper 2024–0848*, Jan 2024. doi:10.2514/6.2024-0848.
- [43] Seydel, R., *Practical Bifurcation and Stability Analysis*, 3rd ed., Interdisciplinary Applied Mathematics, Vol. 5, Springer-Verlag, New York, 2010. doi:10.1007/978-1-4419-1740-9.
- [44] Schumacher Jr, P. W., Sabol, C., Higginson, C. C., and Alfriend, K. T., “Uncertain Lambert Problem,” *Journal of Guidance, Control, and Dynamics*, Vol. 38, No. 9, 2015, pp. 1573–1584. doi:10.2514/1.G001019.
- [45] Arora, N., Russell, R. P., Strange, N., and Ottesen, D., “Partial Derivatives of the Solution to the Lambert Boundary Value Problem,” *Journal of Guidance, Control, and Dynamics*, Vol. 38, No. 9, 2015, pp. 1563–1572. doi:10.2514/1.G001030.
- [46] Sun, F. T., “Analytic Solution for Optimal Two-Impulse 180° Transfer Between Noncoplanar Orbits and the Optimal Orientation of the Transfer Plane,” *AIAA Journal*, Vol. 7, No. 10, 1969, pp. 1898–1904. doi:10.2514/3.5478.
- [47] Zhang, G., Zhou, D., Mortari, D., and Akella, M. R., “Covariance Analysis of Lambert’s Problem via Lagrange’s Transfer-Time Formulation,” *Aerospace Science and Technology*, Vol. 77, Jun 2018, pp. 765–773. doi:10.1016/j.ast.2018.03.039.
- [48] Park, R. S., and Scheeres, D. J., “Nonlinear Semi-Analytic Methods for Trajectory Estimation,” *Journal of Guidance, Control, and Dynamics*, Vol. 30, No. 6, 2007, pp. 1668–1676. doi:10.2514/1.29106.
- [49] Lizia, P. D., Armellin, R., and Lavagna, M., “Application of High Order Expansions of Two-Point Boundary Value Problems to Astrodynamics,” *Celestial Mechanics and Dynamical Astronomy*, Vol. 102, Dec 2008, pp. 355–375. doi:10.1007/s10569-008-9170-5.
- [50] Shu, P., Yang, Z., and Luo, Y.-Z., “Higher-Order Lambert Problem Solution Based on Differential Algebra,” *Journal of Guidance, Control, and Dynamics*, Vol. 45, No. 10, 2022, pp. 1913–1926. doi:10.2514/1.G006558.
- [51] Tsuda, Y., and Scheeres, D. J., “Series Expansion Form of an Approximate State Transition Matrix for Fully Perturbed Orbits,” *Transactions of the Japan Society for Aeronautical and Space Sciences, Aerospace Technology Japan*, Vol. 8, No. ists27, 2010, pp. Pd_53–Pd_60. doi:10.2322/tastj.8.Pd_53.
- [52] Born, G. H., and Kirkpatrick, J. C., “Application of Brouwer’s Artificial-Satellite Theory to Computation of the State Transition Matrix,” NASA Technical Note NASA-TN-D-5934, National Aeronautics and Space Administration, Aug. 1970. Manned Spacecraft Center, Houston, Texas; report number MSC-S-242.